A new Chemical Lagrangian Model of the Stratosphere (CLaMS) 2. Formulation of chemistry scheme and initialization

Daniel S. McKenna, ¹ Jens-Uwe Grooß, Gebhard Günther, Paul Konopka, and Rolf Müller Institute for Stratospheric Chemistry (ICG-1), Jülich, Germany

Glenn Carver

Centre for Atmospheric Science, Department of Chemistry, Cambridge University, Cambridge, England, UK

Yasuhiro Sasano

Global Environment Division, National Institute for Environmental Studies, Tsukuba, Japan

Received 31 October 2000; revised 8 May 2001; accepted 16 July 2001; published 8 August 2002.

[1] The first simulations of stratospheric chemistry using the Chemical Lagrangian Model of the Stratosphere (CLaMS) are reported. A comprehensive chemical assimulation procedure is described that combines satellite, airborne, and balloon-borne tracer observations with results from a two-dimensional photochemical model simulation. This procedure uses tracer-tracer and tracer-potential vorticity mapping techniques. It correctly reproduces all basic features of the observed tracer distribution. This methodology is used to generate the initial composition fields that will be used for subsequent chemical simulations. Results from a 6-day simulation starting on 20 February 1997 show that the simulated HNO₃ distribution displays the correct morphology, although the extremes of the observed HNO₃ distribution are underestimated. The simulated ClO distribution exhibits a similar morphology to the observed Microwave Limb Sounder ClO distribution. Because of unseasonally low temperatures in the arctic lower stratosphere during spring 1997, high levels of chlorine activation are maintained in the simulation, resulting in up to 1.8 ppmv of chemical ozone loss over a 5-week period. Furthermore, simulations show strong spatially inhomogeneous chemical ozone depletion within the polar vortex and show that greatest ozone loss is confined to the vortex core. These results are confirmed by several Halogen Occultation Experiment and ozone sonde profiles, although the minimum ozone concentrations are overestimated. These studies demonstrate that CLaMS is capable of simulating vortex isolation, an essential feature of the polar vortex. INDEX TERMS: 0317 Atmospheric Composition and Structure: Chemical kinetic and photochemical properties; 0341 Atmospheric Composition and Structure: Middle atmosphere—constituent transport and chemistry (3334); 0340 Atmospheric Composition and Structure: Middle atmosphere—composition and chemistry; KEYWORDS: atmosphere, stratosphere, CLaMS, Lagrangian, tracers

1. Introduction

[2] The equations of fluid motion may be formulated as either Eulerian or Lagrangian equations. In the Eulerian approach one considers the changes in fluid properties at fixed points so that the properties at these fixed points may vary due to both the movement of fluid elements with differing properties (advection) or changes in the properties of individual fluid elements. By contrast, in a Lagrangian approach one considers the changes in fluid element properties and the movement of these same fluid elements separately. As such, the Lagrangian approach is usually

conceptually simpler, while the Eulerian approach has historically been more amenable to numerical calculation. Some of the difficulties with Lagrangian formulation arise because the standard theory implies a continuum of infinitesimal air parcels while computation tractability requires that one consider a finite number of air parcels with a parameterization of mixing. Here we present results from a Lagrangian transport scheme with parameterized mixing.

[3] Historically, Lagrangian photochemical models concentrated typically on the chemical evolution along the trajectories of one or a limited number of noninteracting air parcels [Austin et al., 1987]. More recently, there have been attempts to include chemistry with multitrajectory simulations. Lutman et al. [1997] reported stratospheric chemistry simulations for an ensemble of noninteracting air parcels. Collins et al. [1997] calculate tropospheric chemistry along trajectories using a hybrid Lagrangian-

Copyright 2002 by the American Geophysical Union. 0148-0227/02/2000JD000113

¹Now at Atmospheric Chemistry Division, NCAR, Boulder, Colorado,

Eulerian transport scheme that does permit interactions between air parcels. When several air parcels fall within a given grid box, they are partially mixed with the mean concentration of all air parcels that have been advected into that grid box, as part of the transport scheme. Consequently, this gridding procedure introduces mixing for all multiple-occupancy grid boxes regardless of the local flow properties. Thus the impact of this scheme is equivalent to numerical diffusion whenever multiple occupancy occurs. Pierce et al. [1999] have implemented a stratospheric Lagrangian photochemical model in which air masses are traced that have been previously observed by the Halogen Occultation Experiment (HALOE). The mixing between the air parcels is calculated with the socalled Q factor concept [Fairlie et al., 1999]. The advantage of their method is that the initialization of the chemical composition of the air parcels can be derived from the HALOE measurements. However, their model does not apply to areas where air masses not observed by HALOE are found, and the model resolution is limited by the number of HALOE observations.

- [4] McKenna et al. [2002] (hereinafter referred to as part 1) present the Chemical Lagrangian Model of the Stratosphere (CLaMS), a novel Lagrangian formulation of the advection and mixing of trace gases, where mixing is adjustable and linked to regions with strong integral deformation introduced by an adaptive grid scheme. Additionally, unlike the computational cost of Eulerian schemes, the computational cost of transporting many species does not increase significantly with species number. Thus the major increase in computational cost from increased species numbers is due to the chemical integration and not to trace species transport.
- [5] Here we apply CLaMS to the chemical evolution of the 1996-1997 winter North Polar stratosphere with an emphasis on ozone depletion processes within the polar vortex. These studies are confined to the potential temperature level 475 K. We select the winter 1996-1997, as substantial ozone depletion in the arctic lower stratosphere has been reported [e.g., Donovan et al., 1997; Manney et al., 1997; Müller et al., 1997] and it is one of the best observed periods in recent years with several remote sensing and in situ data sets available. The development of temperatures in this winter was atypical. The minimum temperatures in the Northern Hemisphere on the 475-K potential temperature surface were well above the climatological mean during December and early January but decreased below the ice saturation temperature T_{ice} in mid-February, thereafter increasing and remaining above T_{ice} throughout March [Coy et al., 1997] although unseasonably cold. In addition, significant denitrification of >40% has been reported for air masses that were below the ice formation temperature in mid-February [Kondo et al., 2000].
- [6] The aim of this paper is to describe the CLaMS chemical module and the chemical assimulation used to initialize the chemistry. We demonstrate that the simulation of the arctic polar vortex during winter 1996/1997 is consistent with the observations. These simulations show that chlorine activation and chemical ozone loss were both spatially very inhomogeneously distributed inside the polar vortex in 1997.
- [7] Previous chemical transport model (CTM) studies of this winter have been conducted with various focuses.

Hansen and Chipperfield [1999] compare a time series of LIDAR observations made at Andøya (69°N, 16°E) up to early May with simulations by the SLIMCAT model. Over this period, Andøya is mostly located at the vortex edge. They focus on the untypically long existence of the vortex and nitrogen-catalyzed ozone depletion. Ruhnke et al. [1999] compare observations of vertical ClO distribution made at Ny-Ålesund (79°N, 12°E) between 12 and 23 March 1997 with the simulations of the Karlsruhe Simulation of the Middle Atmosphere (KASIMA) model. They concentrate on the reaction kinetics responsible for the partitioning of the active chlorine species. Van den Broek et al. [2000] introduce a new CTM called TM3. They show comparisons with selected ozone sonde profiles and column ozone from the Total Ozone Mapping Spectrometer (TOMS) and the Global Ozone Monitoring Experiment (GOME) and investigate in detail the role of heterogeneous chemistry parameterizations. Their simulation significantly underestimates chemical ozone depletion in the polar vortex, and they attribute this mostly to temperature uncertainties in the European Centre For Medium-Range Weather Forecasts (ECMWF) data. Lefèvre et al. [1998] compare ozone column observations by TOMS and the TIROS Operational Vertical Sounder (TOVS) with simulations of the Reprobus CTM. They point to the large variability in column ozone and attribute part of it to dynamic variability. The two-dimensional (2-D) simulations described here are restricted to the 475-K isentropic surface where observations show both the greatest degree of chemical ozone depletion and the greatest variability in the ozone depletion [Müller et al., 1997]. Ozone changes due to reversible vertical adiabatic displacements do not contribute here because an isentropic vertical coordinate is chosen.

2. Description of the Chemistry Scheme

- [8] The CLaMS model version 1.0 described here contains a comprehensive set of reactions of relevance to the stratosphere (Tables 1 and 2), including full chlorine and bromine chemistry, 36 chemical species, and 115 reactions (including 27 photolysis and 11 heterogeneous reactions). The model chemistry integrations are based on A Selfcontained Atmospheric Chemistry Code (ASAD) Carver et al., [1997], a flexible chemistry module that ensures a simple implementation of changes to the reaction scheme. Such changes do not require modifications of the program code and are therefore less error prone. Since the timescales of chemical reactions in the stratosphere vary over orders of magnitude, the simulation of stratospheric chemistry necessitates the solution of coupled stiff differential equations. ASAD provides several alternative automated approaches to overcome the stiffness problem. Either chemical species are grouped together into chemical families where the intrafamily conversion rates are typically much faster than the net rate of change of a given family, or explicit stiff equation solvers with self-adjusting time step and order are used to solve the reaction scheme.
- [9] The standard routine employing the family concept is the solver IMPACT [Carver and Scott, 2000]. For this solver the chemical species need to be classified into four different groups: (1) regular species, (2) members of a chemical family, (3) constant species, and (4) steady state

Table 1. All Gas-Phase and Photolysis Reactions in the Chemistry Module of CLaMS^a

Reaction Rate Coefficient В1 $O(^{3}P) + O_{2}$ 2.69(-16) $O_2 + O_2$ B2 $O(^{1}D) + O_{2}$ $O(^{3}P) + O_{2}$ 4.54(-11) $O(^{1}D) + H_{2}O$ В3 OH + OH2.20(-10) $O(^{1}D) + H_{2}$ $OH + H_p$ 1.00(-10)B4 $O(^{3}P) + N_{2}$ В5 $O(^{1}D) + N_{2}$ 3.12(-11) $O(^{1}D) + CH_{4}$ OH + CH₃ В6 1.50(-10) $HO_2 + O_2$ B7 $OH + O_3$ 1.84(-14)OH + HO₂ $H_2O + O_2$ 1.68(-10)**B8** В9 OH + H₂O₂ $H_2O + HO_2$ 1.30(-12) $HO_2 + O_3$ B10 $OH + 2O_{2}$ 6.67(-16)B11 $HO_2 + HO_2$ $H_2O_2 + O_2$ 4.62(-12) $NO + O_2$ B12 $O(^3P) + NO_2$ 1.38(-11) $OH + NO_3$ $HO_2 + NO_2$ 2.20(-11)B13 B14 OH + HNO₃ $H_2O + NO_3$ 8.30(-13)B15 $OH + HO_2NO_2$ $NO_2 + H_2O + O_2$ 8.69(-12) $HO_2 + NO$ $NO_2 + OH$ 1.22(-11)B16 B17 $HO_2 + NO_3$ $NO_2 + OH + O_2$ 3.50(-12)B18 $NO + O_3$ $NO_2 + O_2$ 1.66(-15) $NO + NO_3$ $NO_2 + NO_2$ 3.51(-11)B19 $NO_2 + O_3$ $NO_3 + O_2$ 5.74(-19)B20 $CO_2 + H^b$ B21 OH + CO1.54(-13) $OH + CH_4$ $H_2O + CH_3^b$ 3.43(-16)B22 $H_2O + HCO^b$ B23 OH + HCHO 1.00(-11) $H_2O + HCHO + H^b$ B24 OH + CH₃OH 3.34(-13) $OH + CH_3OOH$ $CH_3OO + H_2O$ 7.34(-12)B25 B26 OH + CH₃OOH $CH_2O + OH + H_2O$ 2.99(-12)B27 $HO_2 + CH_3OO$ $CH_3OOH + O_2$ 2.07(-11) $CH_3OO + CH_3OO$ → CH₃OH + HCHO + O₂ 6.46(-13)B28 $NO_2 + HCHO + H^{\tilde{b}}$ B29 CH₃OO + NO1.22(-11)B30 CH₃OOH + C1HC1 + HCHO + OH5.90(-11)B31 $O(^{3}P) + ClO$ C1 + O₂4.26(-11)B32 $OH + Cl_2$ HOC1 + C11.56(-14)**B33** OH + CIO $HO_2 + C1$ 2.85(-11) $HC\bar{l} + O_2$ OH + CIO1.58(-12)B34 B35 OH + HC1 $H_2O + C1$ 4.52(-13) $H_2O + ClO$ B36 OH + HOC1 2.46(-13) $HO_2 + C1$ $HC1 + O_2$ **B37** 4.21(-11)B38 $HO_2 + C1$ OH + ClO4.32(-12)B39 $HO_2 + ClO$ HOC1 + O₂1.59(-11) $C1 + O_3$ $ClO + O_2$ B40 8.46(-12) $HCl + H^b$ B41 $Cl + H_2$ 3.75(-16)B42 $C1 + CH_4$ $HC1 + CH_3^b$ 1.07(-14)HCl + HCOb 6.97(-11)C1 + HCHO B43 $HC1 + HCHO + H^b$ B44 $C1 + CH_3OH$ 5.40(-11)B45 C1 + OC1OClO + ClO7.57(-11) $Cl_2 + OH$ 1.19(-12)C1 + HOC1B46 B47 C1 + HOC1ClO + HCl1.17(-13)B48 Cl + ClONO₂ $Cl_2 + NO_3$ 1.28(-11)2.73(-11)ClO + NOB49 $NO_2 + Cl$ B50 ClO + CH₃OO $C1 + HCHO + HO_2$ 1.29(-12)B51 $O(^{3}P) + BrO$ $Br + O_2$ 6.00(-11) $H_2O + Br$ B52 OH + HBr1.00(-11)B53 $HO_2 + Br$ $HBr + O_2$ 7.47(-13) $HO_2 + BrO$ B54 $HOBr + O_2$ 5.06(-11) $BrO + O_2$ B55 $Br + O_2$ 3.11(-13) $HBr + HCO^{\tilde{b}}$ Br + HCHO B56 3.11(-13)B57 BrO + NO $NO_2 + Br$ 3.23(-11)BrO + ClOBr + OClO 1.49(-11)B58 B59 BrO + ClO $Br + Cl + O_2$ 8.44(-12)B60 BrO + ClO $BrCl + O_2$ 1.75(-12) $Br + Br + O_2$ BrO + BrO2.93(-12)B61 B62 BrO + BrO $Br_2 + O_2$ 2.06(-12)B63 $O(^{3}P) + HOBr$ OH + BrO1.40(-11) $OH + Br_2$ 4.20(-11)HOBr + BrB64 $O(^{3}P) + O_{2} + M$ 2.88(-15)T1 O_3 T2 $OH + NO_2 + M$ HNO₃ 7.15(-12) $HO_2 + NO_2 + M$ 7.74(-13)T3 HO_2NO_2 $HO_2NO_2 + M$ T4 $HO_2 + NO_2$ 7.89(-10)T5 $NO_2 + NO_3 + M$ N_2O_5 1.35(-12)6.10(-10) $N_2O_5 + M$ $NO_2 + NO_3$ T6 $CH_3OO + NO_2 + M$ CH₃O₂NO₂ 4.25(-12)

Table 1. (continued)

$\begin{array}{c ccccccccccccccccccccccccccccccccccc$	Tuble 11 (continued)						
$\begin{array}{cccccccccccccccccccccccccccccccccccc$			Reaction	1	Rate Coefficient		
$\begin{array}{cccccccccccccccccccccccccccccccccccc$	T8	$CH_3O_2NO_2 + M$	\rightarrow	$CH_3OO + NO_2$	1.56(-8)		
$\begin{array}{cccccccccccccccccccccccccccccccccccc$	T9	$ClO + NO_2 + M$	\longrightarrow	ClONO ₂	1.05(-12)		
$\begin{array}{cccccccccccccccccccccccccccccccccccc$	T10	ClO + ClO + M	\longrightarrow	Cl_2O_2	1.17(-13)		
$\begin{array}{cccccccccccccccccccccccccccccccccccc$	T11	$Cl_2O_2 + M$	\rightarrow	2ClO	9.51(-6)		
$\begin{array}{cccccccccccccccccccccccccccccccccccc$	T12	$BrO + NO_2 + M$	\longrightarrow	$BrONO_2$	2.20(-12)		
$\begin{array}{cccccccccccccccccccccccccccccccccccc$	J1	$BrONO_2 + hv$	\rightarrow	$BrO + NO_2$	1.35(-3)		
$\begin{array}{cccccccccccccccccccccccccccccccccccc$	J2	$BrONO_2 + hv$	\longrightarrow	$Br + NO_3$	5.51(-4)		
$\begin{array}{cccccccccccccccccccccccccccccccccccc$	J3	BrCl + hv	\rightarrow	Br + Cl	1.54(-2)		
$\begin{array}{cccccccccccccccccccccccccccccccccccc$	J4	$Cl_2 + hv$	\rightarrow		3.54(-3)		
$\begin{array}{cccccccccccccccccccccccccccccccccccc$	J5	$Cl_2O_2 + hv$	\rightarrow	$C1 + C1OO^b$	2.05(-3)		
$\begin{array}{cccccccccccccccccccccccccccccccccccc$	J6	$CINO_2 + hv$	\rightarrow	$C1 + NO_2$	5.41(-4)		
$\begin{array}{cccccccccccccccccccccccccccccccccccc$	J7	$CIONO_2 + hv$	\rightarrow	$C1 + NO_3$	4.53(-5)		
$\begin{array}{cccccccccccccccccccccccccccccccccccc$	J8	$CIONO_2 + hv$	\rightarrow	$ClO + NO_2$	8.02(-6)		
$\begin{array}{cccccccccccccccccccccccccccccccccccc$	J9	$H_2O_2 + hv$	\rightarrow		7.79(-6)		
$\begin{array}{cccccccccccccccccccccccccccccccccccc$	J10	HCHO + hv	\rightarrow	$HCO^b + H^b$	4.32(-5)		
$\begin{array}{cccccccccccccccccccccccccccccccccccc$	J11	HCHO + hv	\rightarrow	$H_2 + CO$	7.23(-5)		
$\begin{array}{cccccccccccccccccccccccccccccccccccc$	J12	$HO_2NO_2 + hv$	\rightarrow	$HO_2 + NO_2$	6.38(-6)		
$\begin{array}{cccccccccccccccccccccccccccccccccccc$	J13	$HO_2NO_2 + hv$	\longrightarrow	$OH + NO_3$	3.19(-6)		
$\begin{array}{cccccccccccccccccccccccccccccccccccc$	J14	HOBr + hv	\rightarrow	OH + Br	3.28(-3)		
$\begin{array}{cccccccccccccccccccccccccccccccccccc$	J15	HOC1 + hv	\longrightarrow	OH + Cl	4.16(-4)		
$\begin{array}{cccccccccccccccccccccccccccccccccccc$	J16	$HNO_3 + hv$	\rightarrow	$OH + NO_2$	4.99(-7)		
$\begin{array}{cccccccccccccccccccccccccccccccccccc$	J17	$CH_3O_2NO_2 + hv$	\rightarrow	$CH_3OO + NO_2$	9.57(-6)		
$\begin{array}{cccccccccccccccccccccccccccccccccccc$	J18	$CH_3OOH + hv$	\longrightarrow	$HCHO + OH + H^{b}$	7.91(-6)		
$\begin{array}{cccccccccccccccccccccccccccccccccccc$	J19	$N_2O_5 + hv$	\longrightarrow	$NO_3 + NO_2$	2.59(-5)		
$\begin{array}{cccccccccccccccccccccccccccccccccccc$	J20	$NO_2 + hv$	\longrightarrow	$NO + O(^{3}P)$	1.32(-2)		
$\begin{array}{cccccccccccccccccccccccccccccccccccc$	J21	$NO_3 + hv$	\longrightarrow		2.97(-2)		
$\begin{array}{cccccccccccccccccccccccccccccccccccc$	J22	$NO_3 + hv$	\longrightarrow	$NO_2 + O(^3P)$	2.10(-1)		
$\begin{array}{cccccccccccccccccccccccccccccccccccc$	J23	$O_2 + hv$	\longrightarrow	$O(^{3}P) + O(^{3}P)$	7.45(-14)		
J26 OCIO + hv \rightarrow O(3 P) + CIO 1.25(-1)	J24	$O_3 + hv$	\rightarrow	$O_2 + O(^3P)$	5.39(-4)		
	J25	$O_3 + hv$	\rightarrow	$O_2 + O(^1D)$	2.46(-5)		
	J26	OClO + hv	\rightarrow	$O(^{3}P) + ClO$	1.25(-1)		
	J27	$Br_2 + hv$	\rightarrow	Br + Br	4.60(-2)		

^aChemical rate coefficients [cm³ s⁻¹] and thermal decomposition rates (T4, T6, T8, and T11) [s⁻¹] for 200 K temperature and the 50-hPa pressure level (thermolecular rates are already multiplied by the air density) and photolysis rates [s⁻¹] calculated for 60° solar zenith angle, the U.S. standard atmosphere ozone profile, and albedo 0.4. M denotes an additional air molecule (O₂ or N₂) that transfers the reaction energy through collision.

^bModel realization of the species HCO, H, ClOO, and CH₃, which are assumed to react instantaneously to CO+HO₂, HO₂, Cl+O₂, and CH₃O₂, respectively.

species. The chemical families defined for IMPACT here are $O_x (= O_3 + O(^1D) + O(^3P))$, $NO_x (= NO + NO_2 + NO_3)$, ClO_x (= $Cl + ClO + 2Cl_2O_2$), and BrO_x (= Br + BrO). The radicals OH and HO₂ are treated as steady state species; that is, their concentration is determined by chemical production and loss rates only. The explicit stiff solvers provide a more robust result at the expense of higher computing cost. These explicit stiff solvers are used to confirm the results of integrations with the IMPACT scheme. A standard integration time step of 10 min for the family solver IMPACT is required for agreement with the stiff solver integrations. Box model calculations with the IMPACT solver performed in a model intercomparison study showed comparable results with several commonly used chemistry modules [Krämer et al., Intercomparison of stratospheric chemistry models as part of the Germany Ozone Research Program, submitted to Journal of Atmospheric Chemistry, 2001].

[10] The chemical reactions (gas phase and photolysis) are summarized in Table 1. The reaction rate coefficients are taken from current recommendations [*DeMore et al.*, 1997; *Sander et al.*, 2000]. Here the reaction rates are calculated for every hour of the integration. However, this time interval may be varied if required.

Table 2. All Heterogeneous Reactions in the Chemistry Module of CLaMS

	I	Reactio	n	Particle Type
H1	$CIONO_2 + H_2O$	\rightarrow	HOC1 + HNO ₃	NAT, ice, liquid, SAT
H2	$CIONO_2 + HCI$	\longrightarrow	$Cl_2 + HNO_3$	NAT, ice, liquid, SAT
H3	HOC1 + HC1	\longrightarrow	$Cl_2 + H_2O$	NAT, ice, liquid
H4	$N_2O_5 + H_2O$	\longrightarrow	$HNO_3 + HNO_3$	NAT, ice, liquid, SAT
H5	$N_2O_5 + HC1$	\longrightarrow	$CINO_2 + HNO_3$	NAT, ice
H6	$ClONO_2 + HBr$	\longrightarrow	$BrCl + HNO_3$	NAT, ice
H7	$BrONO_2 + HC1$	\longrightarrow	$BrCl + HNO_3$	NAT, ice
H8	HOCl + HBr	\longrightarrow	$BrCl + H_2O$	NAT, ice, liquid
H9	HOBr + HCl	\longrightarrow	$BrCl + H_2O$	NAT, ice, liquid
H10	HOBr + HBr	\longrightarrow	$Br_2 + H_2O$	NAT, ice, liquid
H11	$BrONO_2 + H_2O$	\longrightarrow	$HOBr + HNO_3$	NAT, ice, liquid

[11] The photolysis rates are calculated accounting for spherical geometry [Meier et al., 1982; Lary and Pyle, 1991] with an improved and corrected treatment of the diffuse actinic flux calculation [Becker et al., 2000]. The solar radiation at the top of the atmosphere is the average value over the 11-year solar cycle taken from Lean et al. [1997]. The actinic flux is calculated by the radiative transfer code on the basis of prescribed ozone and oxygen profiles. The ozone distribution may be prescribed by one of two possible approaches, either a single ozone profile or latitude and altitude ozone zonal distributions, currently taken from the Mainz photochemical 2-D model [Gidel et al., 1983; Grooβ, 1996]. A single ozone profile is used for calculations within a small domain, whereas for global calculations the 2-D ozone zonal distributions are used. The photolysis rates are calculated from the absorption cross sections of the current assessment recommendations [DeMore et al., 1997; Sander et al., 2000].

[12] The heterogeneous reaction rates and the microphysics of liquid and solid aerosol are calculated using the scheme developed by Carslaw et al. [1995]. The particle phases considered in these simulations are liquid ternary H₂SO₄/HNO₃/H₂O solution aerosols, solid sulfuric acid tetrahydrate (SAT), nitric acid trihydrate (NAT), and water ice particles. Different phase transition conditions may be selected so that the sensitivity to these microphysical assumptions may be tested. In this study, two different scenarios are considered. For the default case, NAT formation is suppressed and only liquid aerosols exist, forming supercooled ternary solution droplets (STS) below the NAT formation temperature, while in the alternative condensation scenario, NAT is formed from STS droplets upon cooling when an HNO₃ supersaturation with respect to NAT of 10 is reached (~3 K supercooling). The initial density of liquid aerosol particles is set to 10 cm⁻³. The heterogeneous reaction rate coefficient on solid aerosol is determined from the calculated aerosol surface area and the reaction probability of the individual reactions. For the liquid aerosols the uptake of HNO₃, chlorine, and bromine compounds into the liquid phase and the reaction probability determine the rate coefficient. All heterogeneous reactions considered in this study are summarized in Table 2.

3. Initialization

3.1. Tracer-Potential Vorticity Mapping

[13] To integrate a set of chemical equations, initial concentrations of all chemical species at each initial grid

point must be specified. To obtain an initialization for the entire Northern Hemisphere that is consistent with the observed state of the atmosphere at a given time, we have developed a procedure that incorporates all suitable observations employing tracer-tracer and tracer-potential vorticity mapping techniques. PV is derived from meteorological fields taken from United Kingdom Meteorological Office (UKMO) stratospheric analysis [Swinbank and O'Neill, 1994]. By using PV, we are able to generate chemical fields with zonal and meridional gradients that reflect the largescale dynamical structure of the atmosphere. For species where no observations are available, results from a 2-D photochemical model are mapped from 2-D model latitude to PV-based equivalent latitude. Here we employ simulations from the Mainz photochemical 2-D model [Gidel et al., 1983; $Groo\beta$, 1996] sampled for the appropriate initialization time.

[14] For the late winter 1997 simulations, a hemispheric initialization for 20 February 1997 on the 475-K potential temperature level was performed incorporating several satellite and balloon-borne observations. We use the CH₄ data observed by HALOE on the Upper Atmosphere Research Satellite (UARS) [Russell et al., 1993] between 16 February and 17 March on the 475-K potential temperature level. The locations of CH₄ observations are transformed to a synoptic time (20 February 1997) using backward and forward trajectories. These CH₄ data are plotted against the PV at their synoptic locations in Figure 1 (green symbols). Similarly, proxy tracer observations based on observations by the Improved Limb Atmospheric Spectrometer (ILAS) have been added. Because version 5.20 ILAS CH₄ products are not appropriate for use in quantitative analysis [Kanzawa et al., 2002], we use the ILAS N₂O observations in combination with the CH₄/N₂O tracer correlation (see Table 4) to derive the CH₄ mixing ratio. These data are plotted as blue symbols in Figure 1. Low methane mixing ratios are found

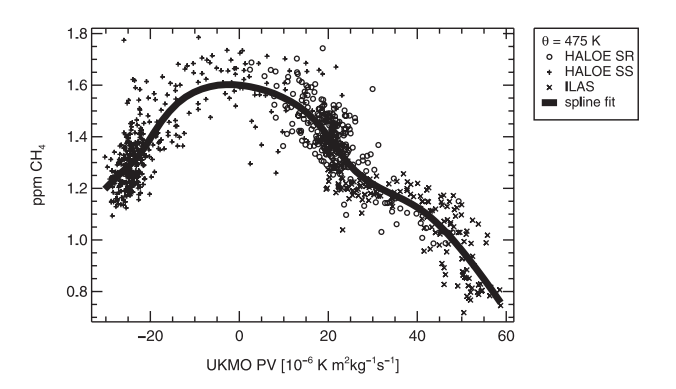


Figure 1. CH₄ initialization on 20 February 1997. Green symbols depict Halogen Occultation Experiment (HALOE) sunset data at $\theta = 475$ -K potential temperature level between 16 February and 17 March 1997 and sunrise data between 16 February and 9 March 1997. Blue symbols show CH₄ mixing ratios derived from Improved Limb Atmospheric Spectrometer (ILAS)N₂O data between 13 and 27 February and from the N₂O/CH₄ correlation in Table 4. Potential Vorticity (PV) of the individual data points is determined by trajectory simulations from the measurements location to 20 February 1997. Also shown is a spline fit to the data that are used for initialization. See color version of this figure at back of this issue.

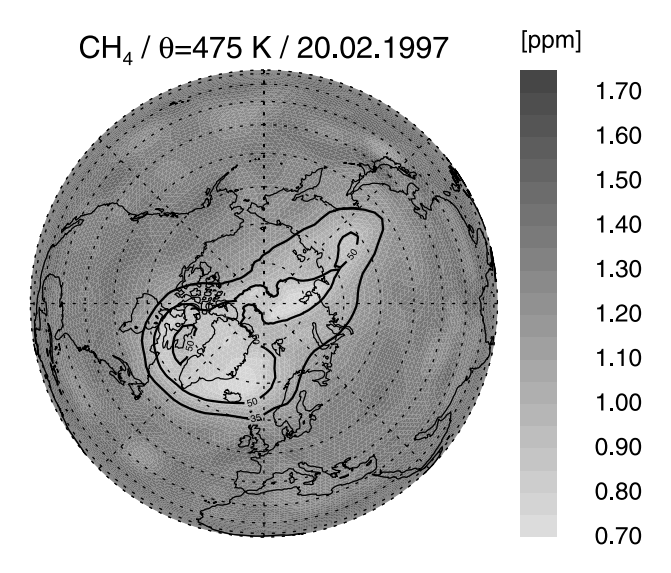


Figure 2. Initialization for CH₄ derived from spline fit correlation with PV on the 475-K potential temperature level mapped on an orthographic projection. Black lines mark the PV contour for 35 PV units (PVU) (vortex edge) and 50 PVU (vortex core region). See color version of this figure at back of this issue.

inside the polar vortex owing to diabatic descent of the vortex air mass over the winter.

[15] A compact relationship may be obtained by ordering CH₄ with respect to PV, as the PV gradients represent a zonally asymmetric vortex boundary. This compact relation enables a spline fit to be determined (red line in Figure 1), which when combined with the appropriate PV field, allows a hemispheric CH₄ initialization to be generated. This CH₄ initialization for 20 February 1997 is depicted in Figure 2. An identical procedure is used to generate H₂O and HCl initializations from HALOE data. The procedure described above is similar to the approach described by Lary et al. [1995], who mapped ozone data onto a 2-D equivalent latitude/potential temperature domain. However, we have found that the method described above does not produce satisfactory results for some species, as the relationship of ozone or HNO₃ with PV (or equivalent latitude) is not compact, particularly at midlatitudes. For those species where a compact relationship with PV cannot be established, an alterantive regridding procedure described in section 3.3 is employed.

3.2. Tracer-Tracer Correlations

[16] The starting point for the generation of fields for N_2O , CFC-11, Cl_v, and Br_v is the initial CH₄ field generated by PV mapping. Correlations between CH₄ and other tracers are derived from balloon-borne observations by cryogenic whole-air samplers and grab samplers [Engel et al., 1997; Bauer et al., 1994]. These correlations, in conjunction with the PV-generated CH₄ field, are used to generate the corresponding tracer fields. The N₂O/CH₄ relation is derived from a vortex flight of the cryogenic whole-air sampler on 11 February. As the correlation between CH₄ and N₂O derived from polar vortex observations is not valid at low latitudes, results from the 2-D model are used at low latitudes. A linear transition from pure 2-D model results to pure tracer correlations is applied between 20°N and 50°N equivalent latitude.

To generate the CFC-11 field, the correlation between CFC-11 and N₂O is in turn deduced from cryosampler and grab-sampler measurements. Similarly, for Cl_v the correlation with N₂O is used. However, at low latitudes the Cl_v amount derived from this vortex correlation is not used; instead, the HCl/Cl_v ratio from the 2-D model is combined with HALOE HCl observations to generate the low-latitude Cl_v field. As above, a linear transition from pure 2-D model results to pure tracer correlations is applied between 20°N and 50°N equivalent latitude. The initialization of the inorganic bromine species Br_v was derived from a correlation with CFC-11 from 1994 [Wamsley et al., 1998]. The Br_v concentrations are scaled to a maximum of 20 parts per trillion by volume (pptv) to account for the annual increase in stratospheric bromine species.

[17] A summary of the data used in the initialization is given in Table 3, and the tracer-tracer correlations employed in this initialization are summarized in Table 4. The concentrations of other chemical species, where no observations were available, and the partitioning within chemical families were taken from 2-D model simulations. The 2-D model data were mapped to equivalent latitude [Lary et al., 1995] calculated from UKMO PV.

3.3. Gridding Procedure

[18] Because ozone does not exhibit a compact relationship with PV, an alternative procedure combining observations from three satellite-borne ozone remote sensors is used for the initialization of ozone. The observations employed are from HALOE V19, the Microwave Limb Sounder (MLS V5) [Barath et al., 1993], and the ILAS v5.20 [Sasano et al., 1999]. These instruments have different observational characteristics that are taken account of in the initialization procedure. HALOE observes 30 profiles daily along two different latitude circles. The ozone profiles have a vertical resolution of 1-2 km and an accuracy of $\sim 5-10\%$. ILAS observes 15 profiles daily between 60°N and 70°N with an accuracy of 4-14%. The MLS observations have a higher density of measurement locations (typically 1200 profiles per day) but a lower accuracy, 10-30%, and a vertical resolution of \sim 4 km in the altitude region considered here. Hypothetical air parcels starting at the positions of the HALOE and ILAS observations and initialized with the observed composition were advected without mixing or chemical evolution forward and backward in time to the assimilation date. Here the HALOE and ILAS data within ±7 days of the assimilation date were used. Similarly, the MLS observations for 20 and 21 February were mapped to the assimilation time (20 February, 1200 UTC) by calculating air parcel advection trajectories from observation locations. Subsequently, the advected HALOE, ILAS, and MLS observations are averaged onto a regular grid, where the weighting ascribed to each data point is the inverse of the reported relative measurement error, thereby accounting for the differing accuracy of the observations. The regular grid averaging follows the method adopted for MLS observations. To achieve higher accuracy, multiple MLS data points need to be averaged. In the literature, daily hemispherical maps of MLS data are typically plotted by averaging the data onto a regular grid using cosine-square weighting with 8° half width in longitude and 3° half width in latitude (M. Santee, private communication, 1999). Here the same

Species	Methoda	Source	Latitude	Date
O ₃	G, A	HALOE (V19) sunrise	10°N-62°N	16.22.3.
		HALOE (V19) sunset	$77^{\circ}S - 31^{\circ}N$	16.217.3.
		MLS (V5)	$34^{\circ}S - 80^{\circ}N$	20.2 21.2.
		ILAS (V5.10) sunrise	$69^{\circ}N - 70^{\circ}N$	13.227.2.
HNO ₃	G, A	MLS (V5)	$34^{\circ}S - 80^{\circ}N$	20.221.2.
,		ILAS (V5.10) sunrise	$69^{\circ}N - 70^{\circ}N$	13.227.2.
CH₄	A, $C(N_2O)$, $C(PV)$	ILAS (V5.10) sunrise	$69^{\circ}N - 70^{\circ}N$	13.227.2.
CH ₄ , HCl, H ₂ O	A, C(PV)	HALOE (V19) sunrise	$10^{\circ}N - 62^{\circ}N$	16.29.3.
		HALOE (V19) sunset	$77^{\circ}S - 31^{\circ}N$	16.217.3.
N_2O	C(CH ₄)	Cryosampler ^b	68°N	11.2.
NO_{ν}	$C(N_2O)$	Kondo et al. [1999]	68°N	10.2., 25.2.
,	Eq	HNO ₃ , model partitioning ^c	$90^{\circ}S - 50^{\circ}N^{d}$,
Cl_{ν}	$C(N_2O)$	Cryo/Grabsampler ^b	68°N	10.2., 11.2., 25.2.
,	Eq	HČl, model partitioning ^c	$90^{\circ}S - 50^{\circ}N^{d}$, ,
CFC-11	$C(N_2O)$	Cryo/Grabsampler ^b	68°N	10.2., 11.2., 25.2.
Br_v	C(CFC-11)	Wamsley et al. [1998]	global	1994 ^é
y	Eq	Mainz 2-D model ^c	$90^{\circ}S - 50^{\circ}N^{d}$	
other	Eq	Mainz 2-D model ^c	$90^{\circ}S - 90^{\circ}N$	

Table 3. Summary of Data Used in Initialization for 20 February 1997

^aInitialization method: G, gridding of the data to regular grid using cosine-square weighting for grid point distance and error weighting; A, advection of the measurements to a synoptic time; C(x), correlation with the quantity x; Eq, equivalent latitude mapping of 2-D model outputs (see text).

method is used, but with 6° half width in longitude and 2° half width in latitude. Figure 3 shows the derived ozone initialization for 20 February 1997.

[19] For HNO₃, outside the vortex we assimilate HNO₃ observations of MLS and ILAS adopting a similar procedure to that described above for ozone. However, inside the vortex, temperatures below the NAT condensation point often occur, so the forgoing procedure will substantially underestimate the total HNO3 concentration. Thus an assimilation is used, based on a NO_v/N₂O correlation determined from balloon profiles measured on 10 and 25 February [Kondo et al., 1999], the N₂O distribution generated by a PV-mapping procedure described in sections 3.1 and 3.2, and the HNO₃ to NO_y partitioning from the Mainz 2-D model. Carrying out this procedure, the total HNO₃ mixing ratio (gas and condensed phase) is estimated to be \sim 11.6 ppbv in the vortex core (PV > 50 PV units (PVU). However, the effects of irreversible denitrification must still be accounted for. Kondo et al. [2000] reported a denitrification of >40% for air masses that had been exposed to synoptic temperatures below Tice for ILAS observations in mid-February. Therefore 15-day diabatic back-trajectories were calculated from assimilation grid points inside the vortex, and the $\mathrm{HNO_3}$ in the air parcels was reduced to 6.5 ppbv if ice formation temperatures on these trajectories were encountered. (Typically, 6.5 ppbv of $\mathrm{HNO_3}$ represent 55% of the vortex $\mathrm{HNO_3}$ mixing ratio derived from tracer correlations; $T_{\mathrm{ice}} = 188.5 \ \mathrm{K}$ for $p = 45 \ \mathrm{hPa}$ and 5.7 ppmv $\mathrm{H_2O}$). The $\mathrm{HNO_3}$ assimilation for 20 February 1997 is plotted in Figure 3 (bottom). The area of denitrification is mainly located within the core of the polar vortex. Since the synoptic temperatures after the second day of the simulation are always above T_{ice} , no additional substantial sedimentation and concomitant denitrification is expected for this simulation. However, it must be noted that the assumed denitrification is somewhat uncertain. The sensitivity to denitrification will be discussed in section 4.3.

4. Simulation of the Stratospheric Arctic Spring 1997

4.1. Short-Term Simulations

[20] Starting on 20 February 1997 and ending on 26 February 1997, chemical simulations of the springtime polar

Table 4. Tracer Correlations Used in the Initialization Procedure^a

[x]	[<i>y</i>]	valid range of [x]	a_0	a_1	a_2	a_3	a_4
CH ₄ , ppm ^b	N ₂ O ppb	0.48 1.84 ppm	-82.71	323.7	-359.3	340.2	-96.37
N ₂ O, ppb ^c	NO_{ν} , ppb	7 145 ppb	10.33	8.798E-3	_	_	_
N ₂ O, ppb ^d	NO_{ν} , ppb	145 220 ppb	5.71	-2.28	11.8	-2.14	-1.04
N ₂ O, ppb ^d	NO_{ν} , ppb	220 315 ppb	20.7	-0.0644	_	_	_
N ₂ O, ppb ^b	Cl_v , ppb	18 313.5 ppb	3344.	1.497	-0.03637	_	_
N ₂ O, ppb ^b	CFC-11, ppt	0 313.5 ppb	8.388	-0.4422	4.056E-3	_	_
CFC-11, ppt ^e	Br_y , ppt	10 260 ppt	20.03	0.0041	-6.631E-4	3.188E-6	-6.713E-9

Tracer correlations derived from the observations using a polynomial spline fit of the form $[y] = \sum_{i=0}^{n} a_i \cdot [x]^i$ and degree $n \le 4$.

^bFrom A. Engel (personal communication, 2000).

^cMainz 2-D model [Gidel et al., 1983; Grooß, 1996].

^dLinear transition between 20°N and 50°N equivalent latitude.

^eBr_y of 1994 scaled to maximum mixing ratios of 20 parts per trillion.

^bFrom A. Engel (personal communication, 2000).

^cMixing line from Kondo et al. [1999].

dEquations from Kondo et al. [1999]

^eEquation from Wamsley et al. [1998] multiplied by a factor of 1.25 to correct for 1994-1997 increase.

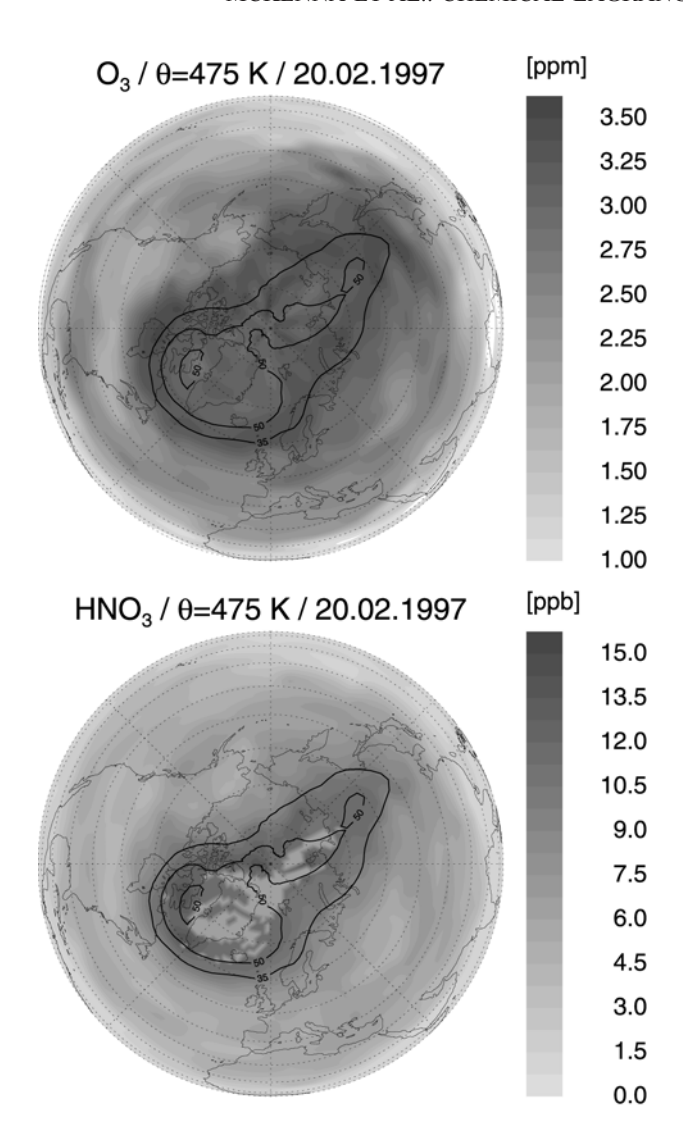


Figure 3. Initialization for (top) O₃ and (bottom) HNO₃ on the 475-K potential temperature level mapped on an orthographic projection. Ozone data are derived from HALOE, ILAS and Microwave Limb Sounder (MLS) data sets, whereas HNO₃ is derived exclusively from MLS. PV contour lines for 35 and 50 PVU are shown in black. See color version of this figure at back of this issue.

vortex composition were performed on the 475-K potential temperature level. The simulations were initialized with the assimilated chemical fields described in section 3. The aim of this simulation is to verify the initialization procedure by comparing species that vary slowly like ozone with observations and to verify the ability of the chemistry scheme to simulate diurnally varying species like ClO. In total, roughly 15,000 adaptive grid points were employed in the simulation with a specified nearest neighbor spacing of 140 km in the Northern Hemisphere. The Lagrangian mixing parameterization was implemented as in part 1 with a mixing time step of 24 hours and a critical Lyapunov exponent $\lambda_c = 1.1 \text{ days}^-$ In contrast to the initialization procedure, the simulations use the wind and temperature data provided from the ECMWF because of their higher resolution of $1.125^{\circ} \times 1.125^{\circ}$ in latitude and longitude and their higher temporal resolution of

- 6 hours. It is desirable to use ECMWF data sets for these simulations, as small-scale temperature variability present in their temperature fields leads to more realistic simulations of polar stratospheric cloud (PSC) formation and subsequent chlorine activation, especially in regions where temperatures are close to the threshold temperatures for PSC formation.
- [21] As discussed in section 3.3, no significant denitrification is expected throughout the simulation period; therefore, the sedimentation of nitrogen-carrying particles may be neglected. Nonetheless, the influence of denitrification will still be felt in these simulations as the initialization is influenced by a period where significant denitrification had already occurred. Although the most realistic initialization includes the effect of prior denitrification, a simulation will also be considered where no initial denitrification is included. Furthermore, as temperatures below the NAT point will occur during the simulations, we also consider two scenarios for PSC composition: either exclusively STS or STS and NAT formation after 3-K supercooling. Over the short simulation period, diabatic descent will be small: therefore isentropic trajectories may be employed.
- [22] So that the quality of these simulations may be assessed, we present comparisons of CLaMS results with several independent satellite observations. Comparisons of ozone, ClO, and HNO3 will be shown that investigate shortterm simulations. Longer-term simulations of ozone will be compared with observations, and the implications for simulated ozone loss will be considered.
- [23] MLS observed the polar vortex between 20 and 26 February, 1997. Observations from 20 and 21 February, 1997 have been used to initialize the CLaMS simulations that are subsequently compared to the MLS observations of 26 February 1997. For the comparison with MLS observations, a CLaMS simulation is integrated as with a normal integration up to the last mixing time step prior to the intercomparison day. Then, box models are initialized with the chemical composition from the CLaMS simulation by sampling the CLaMS irregular grid point nearest to the box model initial positions. These initial positions are chosen so that forward trajectories from these points will coincide with the times and locations of the MLS observations. Box model calculations are performed along each of these trajectories. Figure 4 is a scatterplot of simulated versus observed mixing ratios of ozone, ClO, and HNO₃. Colored symbols indicate vortex observations, and 80% of the simulated ozone mixing ratios lie within the published accuracy of the MLS ozone measurements (\sim 0.4 ppmv). Similarly, the comparison of ClO shows generally good agreement. Figure 4b shows the daylight observations (solar zenith angle of <95°) as ClO at night is converted to Cl₂O₂. Near the vortex edge (green and blue symbols), CLaMS may underestimate the chlorine activation. The agreement for HNO₃ is somewhat worse, especially in the vortex core region (orange symbols) and 50% of the vortex core observations (PV > 50 PVU) are outside the published accuracy of the MLS HNO₃ measurements (1.5 ppbv). Deviations from the one-to-one line in both directions indicate either an inaccuracy in the denitrification estimation or in the calculation of HNO₃ uptake into the PSCs.
- [24] In addition to the scatterplots we show comparisons on hemispheric maps. As discussed in section 3, single MLS observations are usually combined by weighted aver-

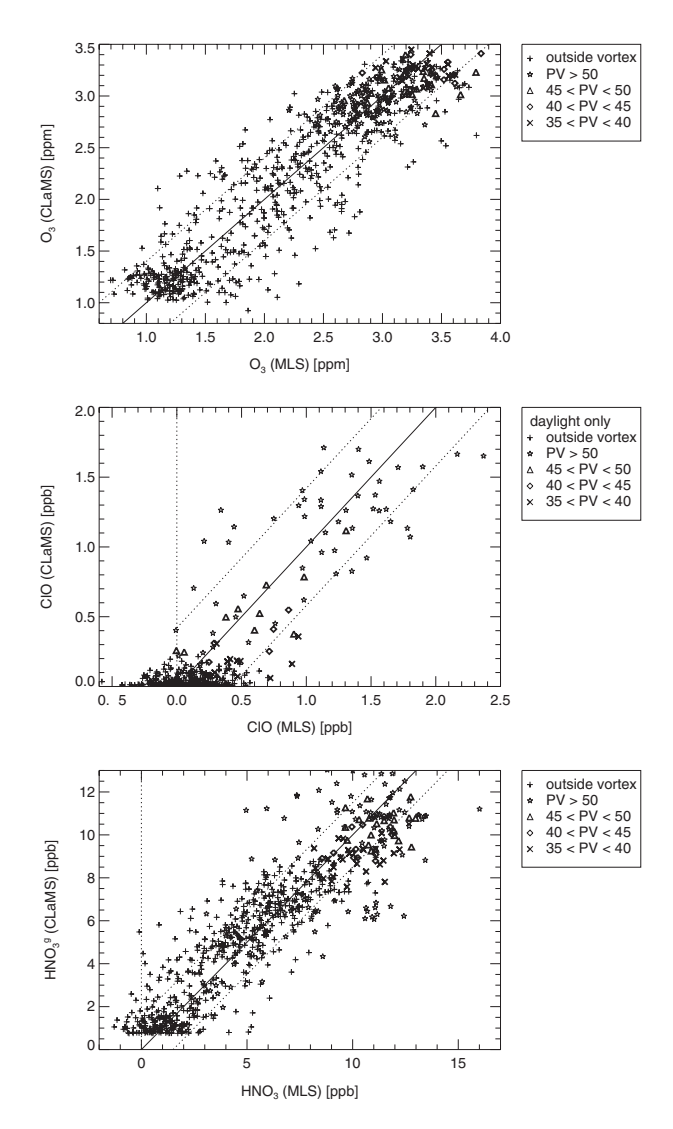


Figure 4. Comparison MLS observations with the Chemical Lagrangian Model of the Stratosphere (CLaMS) simulation for 26 February 1997 for (top) O₃, (middle) ClO, and (bottom) gas-phase HNO₃. MLS observations are plotted against CLaMS simulations for the location and time of the MLS observations. Vortex observations are shown in different colors for different PV. Outside vortex observations are plotted as black symbols. One-to-one line is plotted as a solid line, and the given MLS accuracy is indicated by the dotted lines. See color version of this figure at back of this issue.

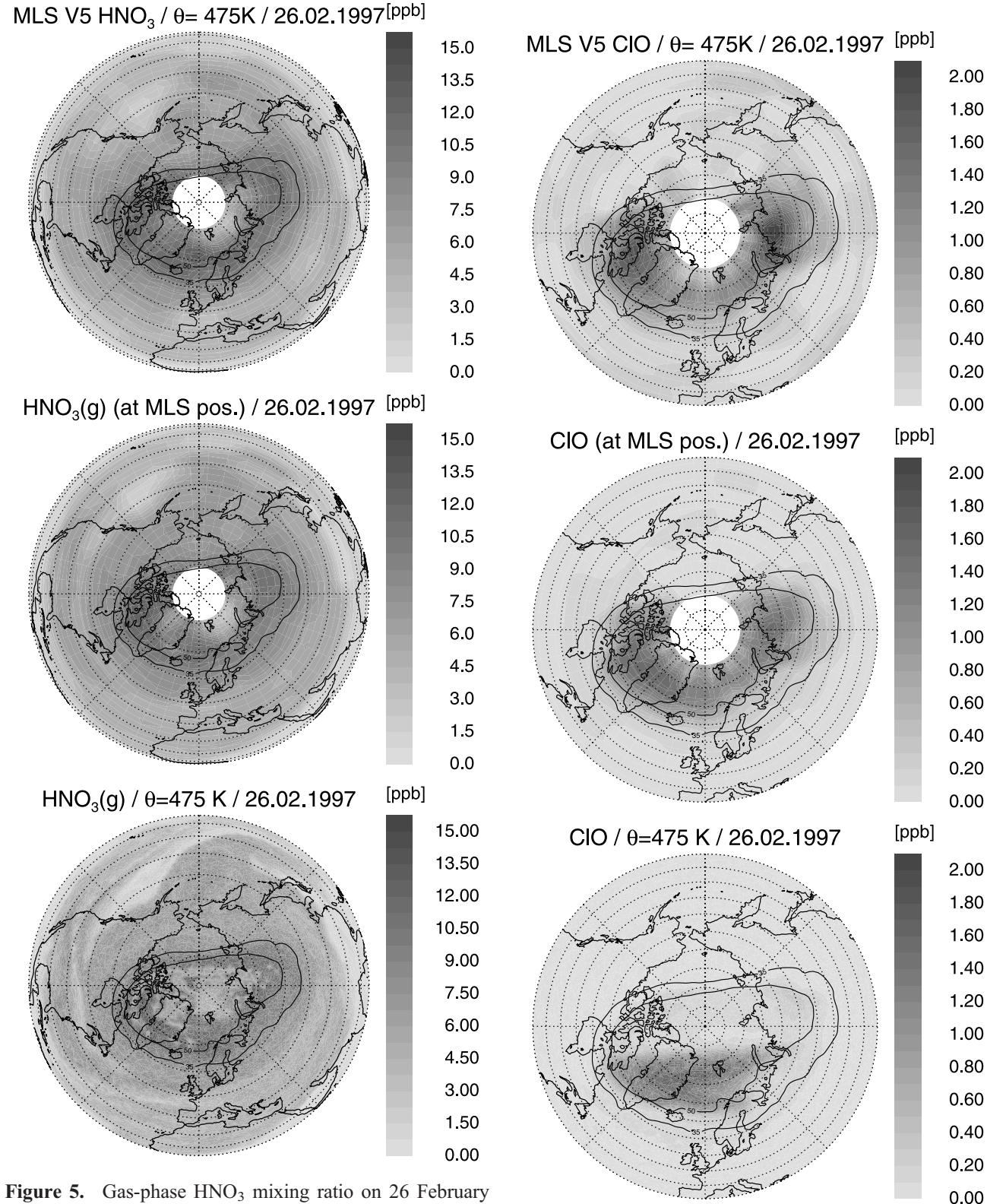
aging onto a regular grid to reduce statistical noise. Thus MLS cannot resolve fine-scale atmospheric structures that fall below the intrinsic MLS grid resolution. Furthermore, MLS observations are usually reported as hemispheric images that summarize observations for a 24-hour period. Thus, when rapid variations occur during a 24-hour period, e.g., photochemical diurnal cycles or PSC condensation events, differences between the asynoptic images and model simulations for the corresponding synoptic time will be difficult to interpret. Therefore, in addition to the relevant synoptic images we will also present images for HNO₃ and ClO from model simulations that have been generated by

the procedure described above to facilitate meaningful comparison with the asynoptic MLS images. From the simulation described above, the concentrations corresponding to the times and locations of the MLS observations are sampled and regridded using the same method as that applied to the MLS observations.

[25] During the time period of the simulations, temperatures below the NAT point occur in the ECMWF analysis, and rapid fluctuations of gas-phase HNO₃ are simulated to occur by condensation onto and evaporation from PSC particles. Figure 5 shows the comparison between MLS measurements (top panel) and simulated gas-phase HNO₃ mixing ratios for the 6-day simulation ending on 26 February 1997: the CLaMS simulation for 26 February 1997 with MLS-type asynoptic sampling and gridding (middle panel) and the same CLaMS simulation with full resolution and synoptic (1200 UT) sampling (bottom panel).

[26] The best agreement with the MLS observations was with the simulation that both included initial denitrification and permitted the exclusive formation of STS PSCs. The simulation with NAT formation from freezing STS droplets led to both a lower minimum HNO3 concentration and a greater geographical extent of low-HNO₃ concentrations than was observed. Thus the exclusive STS scenario gives a more realistic simulation of vortex HNO₃ concentrations. This conclusion is corroborated by the observation of liquidonly (and therefore by implication STS) PSC by LIDAR observations over Spitzbergen between 20 and 28 February [Neuber et al., 1997]. In the areas outside of the polar vortex the HNO₃ mixing ratios mainly represent the initialization. Thus the comparison for midlatitudes provides a confirmation of the initialization method. Many of the most important features of the simulation are reproduced, although there are clear differences between the top and middle panels in Figure 5. The simulated HNO₃ in the collar region is underestimated, while the extent of the low-HNO₃ region over Greenland is overestimated. Nevertheless, one may consider this as a reasonable HNO₃ simulation given the caveats needed on both the observations and simulations. Thus we see from the degradation of the high-resolution simulation, when it is regridded onto the MLS grid, that satellite instruments with observational characteristics similar to MLS will observe only the largest-scale filamentary structures.

[27] In Figure 6 the asynoptic image of the MLS ClO data (top panel), including only daytime measurements (between 0800 and 1900 h local solar time), is compared with the synoptic CLaMS image (bottom panel). Clearly, for a diurnally varying species like ClO the comparison between the asynoptic image and the synoptic image is even less meaningful. By contrast, the MLS-type sampling (middle panel) exhibits many features evident in the observations (top panel). The pattern of ClO inside the vortex core region (PV \geq 50 PVU) is well simulated, as is the meridional gradient near the vortex edge (50 PVU ≥ PV ≥ 35 PVU) and the poleward decrease at high solar zenith angles. Still, the area of activated chlorine in the simulation does not extend as far into the vortex edge region as the observations indicate. Moreover, the simulated maximum ClO concentration in the 90°E local maximum substantially underestimates the reported concentration, and an 80°W local maximum is more elongated in the simulations than in the observations. However, Figure 4 (middle panel) shows that



1997. (top) MLS measurements as typically plotted. (middle) Model results of the same locations in space and time as the MLS observations, plotted with the same gridding procedure as above. (bottom) Model results for full CLaMS resolution. See color version of this figure at back of this issue.

Figure 6. As in Figure 5, but for ClO mixing ratio. (top) Daytime MLS measurements (between 0800 and 1900 local solar time). (middle) Model results for the MLS positions. (bottom) Model results at 1200 UTC for full resolution. See color version of this figure at back of this issue.

for data points with MLS-observed ClO of >1.3 ppbv, only two simulated data points underestimate the observed ClO amount by more than the published MLS accuracy.

[28] Both the model results and the MLS data indicate an almost complete chlorine activation in the vortex core region (PV \geq 50 PVU) on 26 February. Outside the vortex core, there is little chlorine activation, resulting in low ClO mixing ratios. The low ClO mixing ratios toward the North Pole are due to the lack of daylight at very high latitudes. Inside the vortex core region, there are some differences in the location of activated chlorine that are yet unclear. However, the results of the simulation generally seem to be comparable to the measurements of ClO and HNO3.

4.2. Continuation of Simulation

[29] The daily simulated loss of ozone is only \sim 3% at its maximum and is therefore too small to be detected with certainty over a 6-day period with current observational technology. Thus the simulations are extended out to 5 weeks (31 March, 1997) so that ozone loss deduced from observations may be compared with the simulated ozone loss. Over this longer-term simulation period, diabatic descent or ascent may be significant; for example, in the tropical and subtropical regions, diabatic trajectory calculations indicate that air parcels will rise by 40-50 K over a 5-week period. However, inside the vortex (PV > 35 PVU) for this period, vertical displacement was <15 K, i.e., ~ 0.6 km. Thus, although the isentropic approximation may be poor outside the polar vortex, it is a reasonable assumption inside the vortex. Therefore only vortex results for the isentropic simulations will be considered. Further, the validity of the isentropic approximation over the whole simulation period is confirmed by the comparison of simulated and observed CH₄. In order to compare the asynoptic HALOE observations with the synoptic model simulations, hypothetical air parcel trajectories starting at the time and location of the HALOE observations are calculated, and their corresponding locations are determined at the requisite

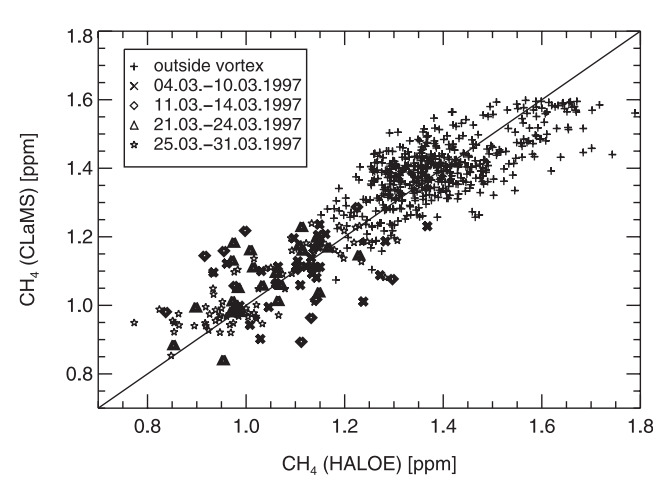


Figure 7. Comparison of CH₄ mixing ratios observed by HALOE with the CLaMS simulation for all HALOE data points within the simulation period. Vortex observations are shown in different colors indicating the time of the observation. Outside vortex observations are plotted as black symbols. See color version of this figure at back of this issue.

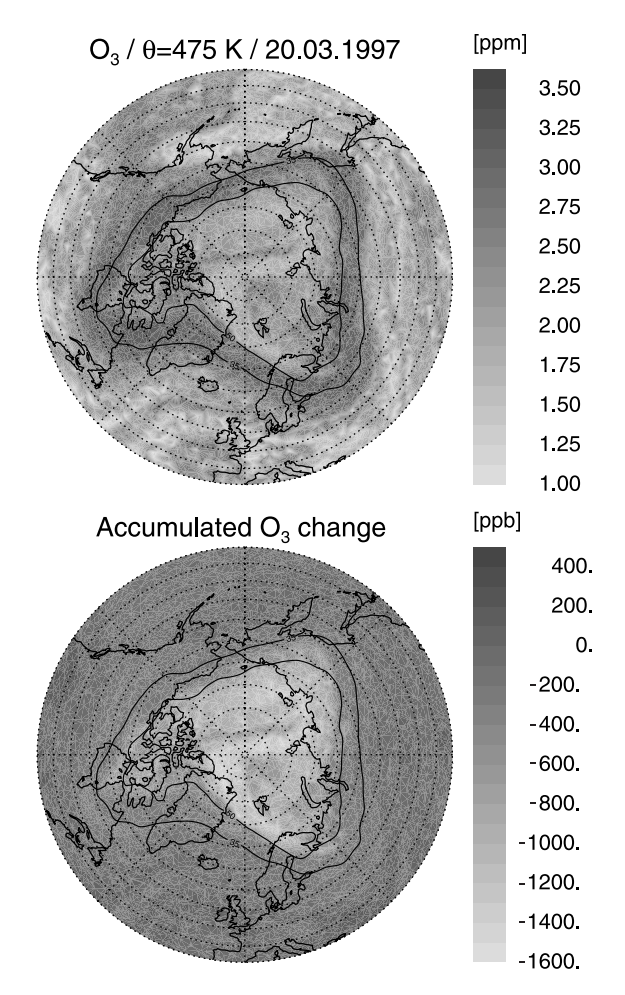


Figure 8. Results of the simulation for 20 March 1997 on the 475-K isentropic level. (top) Simulated ozone mixing ratio. (bottom) Accumulated chemical ozone change since 20 February 1997. See color version of this figure at back of this issue.

synoptic time. The average simulated CH_4 mixing ratio for all air parcels within a 150-km radius (r) of these locations is then calculated with a 1/r weighting. Figure 7 is a scatterplot of CH_4 observed by HALOE versus the simulated value for the locations of the observations for the whole simulation period. Vortex observations are colored, and black symbols show outside vortex observations. The deviation from the one-to-one line is within the range expected from the initialization procedure (see Figure 1).

[30] To derive the accumulated chemical ozone loss from the simulation, an additional passive tracer has been initialized exactly like the ozone mixing ratio and exposed to the same advection and mixing procedure as the regular chemical species but without chemical change, similar to other CTM studies [e.g., *Lefèvre et al.*, 1998; *Hansen and Chipperfield*, 1999]. The difference between the passive ozone tracer and simulated ozone is a measure of the accumulated chemical ozone loss. Figure 8 shows the simulated ozone mixing ratio for 20 March 1997 (top panel) and the accumulated ozone loss since 20 February (bottom panel). Figure 9 shows the same for the end of the 5-week simulation period (31 March). The simulation suggests that two largely separated vortex air masses have developed in spring 1997: the vortex core (PV \geq

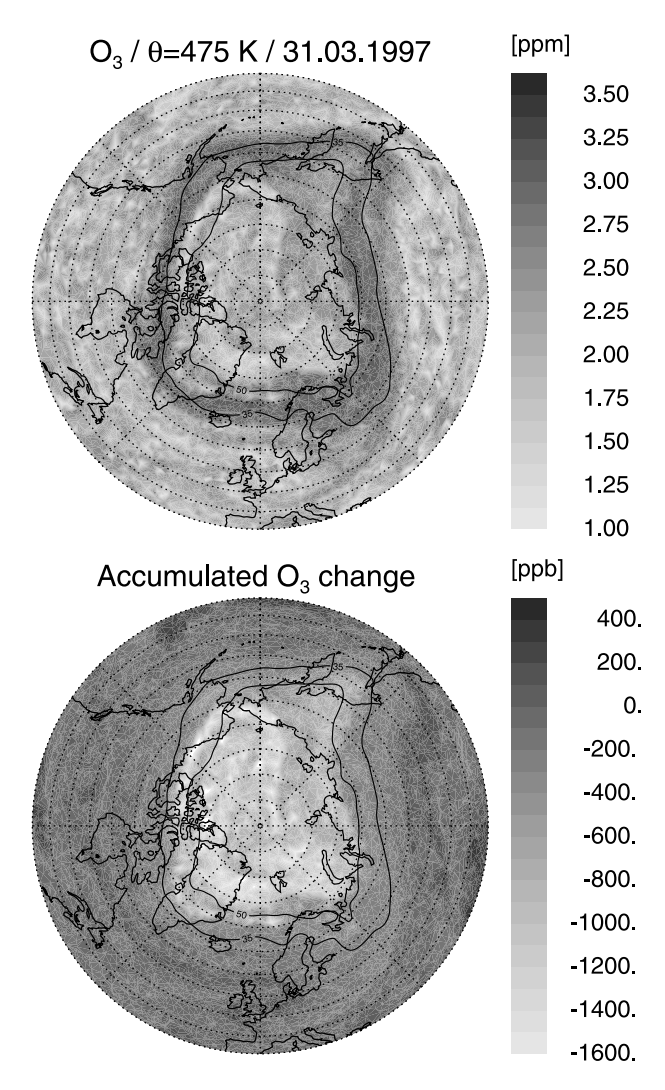


Figure 9. As in Figure 8, but for 31 March 1997. See color version of this figure at back of this issue.

50 PVU) with a large ozone loss and the outer vortex (50 $PVU \ge PV \ge 35 PVU$) with moderate ozone loss. However, the simulated ozone loss in the vortex core region is not uniformly distributed, and regions of intermediate ozone depletion are evident in the simulations of the core region. This is most clearly seen in the results of the simulations for 20 March (Figure 8). This result is consistent with the findings from the 1996/1997 Match campaign [Schulz et al., 2000] that greater ozone loss rates are found near the vortex core. By 30 March the average accumulated chemical ozone loss ($\pm 1\sigma$) was 0.9 ± 0.3 ppmv or $30 \pm 11\%$ for the simulation of the 475-K level in the vortex core region (PV > 50 PVU). The maximum simulated loss in individual air parcels in the vortex core is 1.8 ppmv, i.e, up to 60%. By contrast, for the same time period the average simulated ozone loss in the outer vortex (50 PVU > PV > 35 PVU) is $13 \pm 7\%$. These maximum values of accumulated loss are not in agreement with those reported by Van den Broek et al. [2000], who simulate only about half of these values. These distinct ozone loss regions within the polar vortex arise because of the differences in temperature history between the core and outer vortex. Throughout February and March the coldest air in the polar vortex is always near the vortex

core, and only this air is cold enough to experience both denitrification (as reflected in the HNO₃ initialization) and heterogeneous chlorine activation. Thus the inorganic chlorine in the outer vortex is only partially activated (compare Figure 6).

[31] The simulation of inhomogeneous ozone depletion within the polar vortex is consistent with observations. Figure 10 shows a scatterplot of measurements inside the vortex from HALOE, ILAS, and balloon-borne ozone sondes for the last week of the simulation period (25 to 31 March 1997) compared with simulated ozone mixing ratios for exactly the same time and the same location. This comparison confirms the variability of ozone mixing ratios within the polar vortex. However, there are HALOE and ozone sonde observations of ozone mixing ratios below 1.5 ppmv that are not reproduced by the simulation. These discrepancies are found only for the vortex core. The maximum discrepancy is 1.2 ppmv. The ILAS measurements of ozone mixing ratios in the region with the greatest ozone depletion (vortex core) show larger values than HALOE and ozone sonde measurements and, accordingly, seem to agree well with the simulation. However, from ILAS validation [Sugita et al., 2002], there is an indication of a possible small bias toward larger values in the ILAS ozone data, especially below 15 km. This tendency is especially pronounced for the cases with a very shallow layer of very low ozone because of the effective vertical resolution of ILAS (T. Sugita, personal communication, 2001). This may partly explain the discrepancies between ILAS ozone and the ozone sonde observations. Assuming that the lower ozone mixing ratios observed by HALOE and ozone sondes at the simulation level are more accurate, the simulation underestimates ozone depletion for some areas in the vortex core. Possible reasons for such a discrepancy could be an underestimation of denitrification leading to a shorter period of ozone

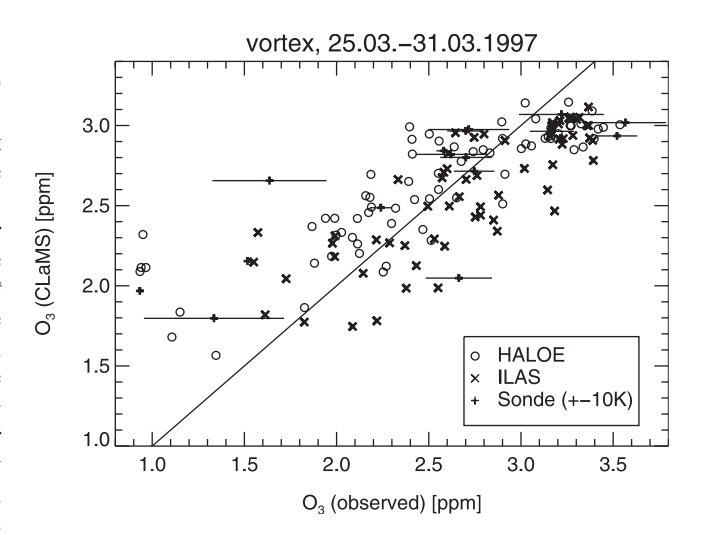


Figure 10. Comparison of O_3 mixing ratios observed by HALOE, ILAS, and ozone sondes within the last week of the CLaMS simulation (25–31 March 1997). For the ozone sondes (red symbols) the average standard deviation in the interval $\theta = 475 \pm 10$ K is depicted. One-to-one line is plotted as a solid line. See color version of this figure at back of this issue.

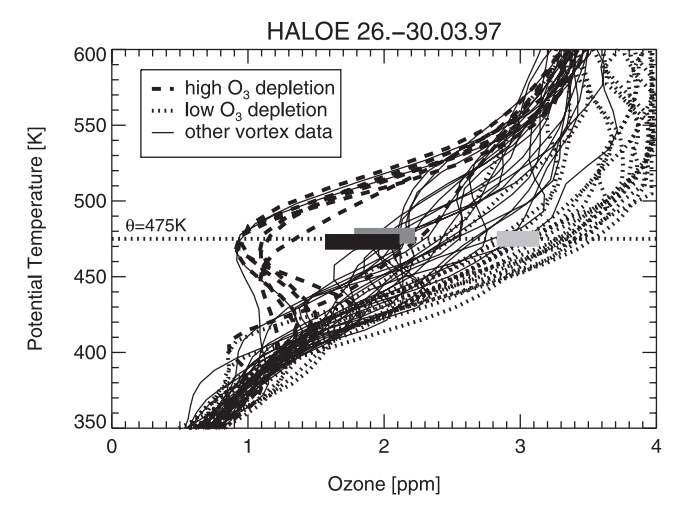


Figure 11. HALOE ozone profile measurements inside the vortex between 26 and 30 March 1997. Color indicates the simulated ozone depletion. Blue lines show HALOE data at locations of high ozone depletion, red lines show HALOE data at locations of low ozone depletion, and black lines show the remaining vortex data (see text for details). Colored bars show the range of the simulated ozone mixing ratios interpolated to the HALOE measurement locations. Blue bar corresponds to the blue HALOE profiles for the reference simulation with denitrification. Green bar corresponds to the same for the sensitivity calculation without denitrification. Orange bar corresponds to the red HALOE profiles (for simulations both with and without denitrification). See color version of this figure at back of this issue.

depletion or an underestimation of ozone loss rates in spring [e.g., *Becker et al.*, 1998, 2000, and references therein].

- [32] Indications of the spatial segregation of the ozone loss within the core and outer vortex as well as the vertical extent of the strong ozone depletion were also seen in the HALOE observations. Figure 11 shows all ozone profiles obtained by HALOE inside the polar vortex between 26 and 30 March. The CLaMS simulation of accumulated ozone depletion is compared to the HALOE ozone profiles corresponding to the adjusted synoptic observation locations (see above).
- [33] In Figure 11, for those locations where the simulated ozone loss is found to be >1 ppmv, the corresponding HALOE profile is shown in blue, while for those locations where the simulated ozone loss is <0.4 ppmv, the corresponding HALOE profile is shown in red. The remaining vortex profiles are shown in black. All but one of the ozone profiles predicted to exhibit the greatest ozone loss (blue lines) show a layer of very low ozone with mixing ratios close to 1 ppmv. In an earlier study, *Müller et al.* [1997] have shown, by considering the relationship between ozone and HF, that these profiles have experienced significant chemical ozone depletion, strongly supporting the interpretation presented here.
- [34] Furthermore, Figure 11 shows the range of simulated ozone mixing ratios corresponding to the two distinct groups of ozone profiles as horizontal bars of the same color. These first simulations with CLaMS overestimate the ozone concentration in this low-ozone layer and by implication overestimate the degree of ozone loss sustained in

this layer. However, it is striking that they successfully predict those HALOE profiles with a strong signature of ozone loss, suggesting that the transport and many aspects of the chemistry are well simulated in the vortex core. Furthermore, in the simulation the range of ozone values in the vortex edge region where simulated ozone depletion was less is approximately reproduced (Figure 11, red profiles). Besides two profiles, CLaMS reproduces the range of ozone mixing ratios below 3.2 ppmv. However, observed ozone values with mixing ratios above 3.2 ppmv cannot be simulated. This may either be due to the initialization procedure or due to the influence of diabatic descent in the outer vortex.

[35] In summary, despite the limitations mentioned above, this first 5-week simulation of the dynamical and chemical evolution of the 1997 later winter/early spring ozone loss on the 475-K potential temperature level may be considered successful.

4.3. Sensitivity Studies

- [36] The sensitivity of the simulated ozone loss to the denitrification initialization was tested by a calculation where the initial denitrification was not included. Here the simulated ozone depletion was similarly distributed; that is, two distinct air masses in the vortex are also evident. However, under such conditions the average accumulated ozone loss in the vortex core is 20-30% lower than in the case with denitrification, while the outer vortex ozone losses are unchanged. Furthermore, a simulation was performed in which denitrification was assumed to be stronger and to extend over a larger geographical region. This was done by reducing the HNO3 mixing ratio to 5.0 ppbv for all air parcels exposed to minimum temperatures below $T_{\rm ice} + 2 \text{ K}$ in the back-trajectory of the ini-tialization procedure. This assumption leads to an overestimation of the denitrification that is evident from an intercomparison with MLS and ILAS HNO₃ data. With respect to the standard simulation, the average ozone depletion increased by 0.3 ppmv or 10% in the vortex core and by 0.07 ppmv or 2.3% in the vortex edge region. The discrepancy in the comparison with the HALOE ozone data was slightly reduced, but the maximum discrepancy was still as large as 1.0 ppmv.
- [37] Sensitivity of the ozone loss to the microphysical assumptions was also tested; instead of exclusively STS PSCs, as in the standard simulation, an additional simulation with NAT particle formation at $T_{\rm NAT}$ without supersaturation was carried out. There were obvious differences in the gas-phase HNO₃ during the early phase of the simulation. By the end of March the ozone depletion in the vortex core increased with respect to the standard simulation on average by 0.17 ppmv or 5%. In the vortex edge region the different microphysical assumptions had no significant effect. Thus, for this particular simulation, the assumptions on particle formation do not substantially influence the simulated ozone loss.

5. Summary and Conclusions

[38] Here we present first results from a new chemical transport model that used a Lagrangian formulation of transport and a mixing parameterization based on concepts from dynamical system analysis described in part 1.

- [39] In this study, combined results for a chemical assimilation/simulation on the 475-K isentropic level for the period beginning late February and ending late March 1997 have been presented. Diabatic heating calculations indicate net vertical displacements of up to 15 K over the simulation period (i.e., only 0.6 km) so that within the vortex the assumption of isentropic motion is justified. It has been shown that when satellite observations are reported in an asynoptic format, it is essential for a meaningful comparison to process similarly the simulated tracer fields. The simulations of HNO₃ reproduce the most prominent observed HNO3 features, although extreme values are underestimated. Filamentary structures in the CLaMS simulations are eliminated by the MLS gridding procedures. Thus such features in the real atmosphere are unlikely to be detected by current satellite technology.
- [40] Simulations of CIO show good qualitative and spatial agreement, although the largest CIO values reported by MLS are underestimated by \sim 30%.
- [41] Simulations over a 5-week period indicate that within the vortex, two distinct ozone loss regions develop: the vortex core with sustained losses of up to 60% and the outer vortex with smaller ozone losses of ~13%. Comparisons of the simulated ozone values with HALOE profiles at the end of the simulation period demonstrate that the CLaMS simulations indicated significant ozone loss when and only when significant ozone loss was evident in the satellite profiles. The strong ozone depletion in the vortex core derived from HALOE observations is underestimated by the simulation by up to 1.2 ppmv. However, regions of intermediate and low ozone depletion are well simulated.
- [42] In summary, we have demonstrated that CLaMS can successfully simulate polar chemistry in detail for dynamically complex situations and faithfully reproduces important observed features of the chemical state of the springtime polar vortex.
- [43] **Acknowledgments.** The authors thank Michelle Santee for providing MLS version 5 data. We acknowledge the HALOE science team led by James M. Russell III for providing HALOE (V19) data. Further, we used data that were obtained with the Improved Limb Atmospheric Spectrometer (ILAS, V5.20) developed by the Environment Agency of Japan (EA). ILAS was on board the ADEOS satellite launched by the National Space Development Agency of Japan (NASDA), and ILAS data were processed at the ILAS Data Handling Facility, National Institute for Environmental Studies (NIES). We thank Takafumi Sugita for discussion on ILAS measurements and for a preprint of the ILAS ozone validation paper. The United Kingdom Meteorological Office and the European Centre for Medium-Range Weather Forecasts provided stratospheric wind and temperature data. Andreas Engel made the whole-air sampler data available. Ozone sonde data from the following principal investigators have been used: Geir O. Braathen, Hans Fast, Hartwig Gernandt, Manuel Gil, Hiroshi Kanzawa, Esko Kyrö, and Ib S. Mikkelsen. We thank Ken Carslaw for making his heterogeneous chemistry module available to us. Also, we thank Jürgen Ankenbrand and Nicole Thomas for their programming support. This work was funded by the German Bundesministerium für Bildung, Wissenschaft, Forschung und Technologie under contract 01 LO 9525/0.

References

- Austin, J., R. C. Pallister, J. A. Pyle, A. F. Tuck, and A. M. Zavody, Photochemical model comparisons with LIMS observations in a stratospheric trajectory coordinate system, Q. J. R. Meteorol. Soc., 113, 361– 302, 1087
- Barath, F. T., et al., The Upper Atmosphere Research Satellite Microwave Limb Sounder instrument, *J. Geophys. Res.*, 98, 10,751–10,762, 1993.

- Bauer, R., A. Engel, H. Franken, E. Klein, G. Kulessa, C. Schiller, and U. Schmidt, Monitoring the vertical structure of the arctic polar vortex over northern Scandinavia during EASOE: Regular N₂O profile observations, *Geophys. Res. Lett.*, 21, 1211–1214, 1994.
- Becker, G., R. Müller, D. S. McKenna, M. Rex, and K. S. Carslaw, Ozone loss rates in the arctic stratosphere in the winter 1991/92: Model calculations compared with Match results, *Geophys. Res. Lett.*, 25, 4325–4328, 1998
- Becker, G., J.-U. Grooß, D. S. McKenna, and R. Müller, Stratospheric photolysis frequencies: Impact of an improved numerical solution of the radiative transfer equation, *J. Atmos. Chem.*, *37*, 217–229, 2000.
- Carslaw, K. S., B. P. Luo, and T. Peter, An analytical expression for the composition of aqueous HNO₃-H₂SO₄-H₂O stratospheric aerosols including gas phase removal of HNO₃, *Geophys. Res. Lett.*, 22, 1877–1880, 1005
- Carver, G. D., and P. A. Scott, IMPACT: An implicit time integration scheme for chemical species and families, *Ann. Geophys.*, 18, 337–346, 2000.
- Carver, G. D., P. D. Brown, and O. Wild, The ASAD atmospheric chemistry integration package and chemical reaction database, *Comput. Phys. Commun.*, 105, 197–215, 1997.
- Collins, W. J., D. S. Stevenson, C. E. Johnson, and R. G. Derwent, Tropospheric ozone in a global-scale three-dimensional Lagrangian model and its response to NO_x emission controls, *J. Atmos. Chem.*, 26, 223–274, 1997.
- Coy, L., E. Nash, and P. Newman, Meteorology of the polar vortex: Spring 1997, *Geophys. Res. Lett.*, 24, 2693–2696, 1997.
- DeMore, W. B., S. P. Sander, D. M. Golden, R. F. Hampson, M. J. Kurylo, C. J. Howard, A. R. Ravishankara, C. E. Kolb, and M. J. Molina, Chemical kinetics and photochemical data for use in stratospheric modeling, JPL Publ., 97–4, 1997.
- Donovan, D. P., et al., Ozone, column ClO, and PSC measurements made at the NDSC Eureka observatory (80°N, 86°W) during the spring of 1997, *Geophys. Res. Lett.*, 24, 2709–2712, 1997.
- Engel, A., U. Schmidt, and R. A. Stachnik, Partitioning between chlorine reservoir species deduced from observations in the arctic winter stratosphere, *J. Atmos. Chem.*, 27, 107–126, 1997.
 Fairlie, T. D., R. B. Pierce, J. A. Al-Saadi, W. L. Grose, J. M. Russell, M. H.
- Fairlie, T. D., R. B. Pierce, J. A. Al-Saadi, W. L. Grose, J. M. Russell, M. H. Proffitt, and C. R. Webster, The contribution of mixing in Lagrangian photochemical predictions of polar ozone loss over the arctic in summer 1997, J. Geophys. Res., 104, 26,597–26,609, 1999.
- Gidel, L. T., P. J. Crutzen, and J. Fishman, A two-dimensional photochemical model of the atmosphere, 1, Chlorocarbon emissions and their effect on stratospheric ozone, *J. Geophys. Res.*, 88, 6622–6640, 1983.
- Grooß, J.-U., Modelling of stratospheric chemistry based on HALOE/ UARS satellite data, dissertation, Universität Mainz, Mainz, Germany, 1996.
- Hansen, G., and M. P. Chipperfield, Ozone depletion at the edge of the arctic polar vortex 1996/1997, *J. Geophys. Res.*, 104, 1837–1845, 1999.
 Kanzawa, H., et al., Validation and data characteristics of nitrous oxide and methane profiles observed by the Improved Limb Atmospheric Spectrometer (ILAS) and processed with the version 5.20 algorithm, *J. Geophys. Res.*, 107, 10.1029/2001JD000881, in press, 2002.
- Kondo, Y., et al., NO_y-N₂O correlation observed inside the arctic vortex in February 1997: Dynamical and chemical effects, *J. Geophys. Res.*, 104, 8215–8224, 1999.
- Kondo, Y., H. Irie, M. Koike, and G. Bodecker, Denitrification and nitrification in the arctic stratosphere during the winter of 1996–1997, Geophys. Res. Lett., 27, 337–340, 2000.
- Lary, D. J., and J. A. Pyle, Diffuse radiation, twilight, and photochemistry, I, J. Atmos. Chem., 13, 373–406, 1991.
- Lary, D. J., M. P. Chipperfield, J. A. Pyle, W. A. Norton, and L. P. Riishoj-gaard, Three-dimensional tracer initialization and general diagnostics using equivalent PV latitude-potential-temperature coordinates, Q. J. R. Meteorol. Soc., 121, 187–210, 1995.
- Lean, J. L., G. J. Rottman, H. L. Kyle, T. N. Woods, J. R. Hickey, and L. C. Puga, Detection and parameterization of variations in solar mid- and near-ultraviolet radiation (200–400 nm), J. Geophys. Res., 102, 29,939–29,956, 1997.
- Lefèvre, F., F. Figarol, K. S. Carslaw, and T. Peter, The 1997 arctic ozone depletion quantified from three-dimensional model simulations, *Geophys. Res. Lett.*, 25, 2425–2428, 1998.
- Lutman, E. R., J. A. Pyle, M. P. Chipperfield, D. J. Lary, I. Kilbane-Dawe, J. W. Waters, and N. Larsen, Three-dimensional studies of the 1991/1992 Northern Hemisphere winter using domain-filling trajectories with chemistry, J. Geophys. Res., 102, 1479–1488, 1997.
- Manney, G. L., L. Froidevaux, M. L. Santee, R. W. Zurek, and J. W. Waters, MLS observations of arctic ozone loss in 1996–1997, *Geophys. Res. Lett.*, 24, 2697–2700, 1997.
- McKenna, D. S., P. Konopka, J.-U. Grooß, G. Günther, R. Müller, R.

- Spang, D. Offerman, and Y. Orsolini, A new Chemical Lagrangian Model of the Stratosphere (ClaMS), 1, Formulation of advection and mixing, *J. Geophys. Res.*, 107, 10.1029/2000JD000114, in press, 2002.
- Meier, R. R., D. E. Anderson Jr., and M. Nicolet, Radiation field in the troposphere and stratosphere from 240–1000 nm, I, General analysis, *Planet. Space Sci.*, 30, 923–933, 1982.
 Müller, R., J.-U. Grooß, D. McKenna, P. J. Crutzen, C. Brühl, J. M. Russell,
- Müller, R., J.-U. Grooß, D. McKenna, P. J. Crutzen, C. Brühl, J. M. Russell, and A. F. Tuck, HALOE observations of the vertical structure of chemical ozone depletion in the arctic vortex during winter and early spring 1996–1997, *Geophys. Res. Lett.*, 24, 2717–2720, 1997.
- Neuber, R., P. von der Gathen, J. Biele, J. Rosen, H. Gernandt, The effect of different PSC particles on local ozone depletion during arctic winter 1996/97, in *Polar Stratospheric Ozone*, edited by N. R. P. Harris, I. Kilbane-Dawe, and G. T. Amanatidis, pp. 159–162, Eur. Comm., Brussels 1997
- Pierce, R. B., J. A. Al-Saadi, T. D. Fairlie, J. R. Olson, R. S. Eckman, G. S. Lingenfelser, W. L. Grose, and J. M. Russell, Large-scale stratospheric ozone photochemistry and transport during the POLARIS campaign, J. Geophys. Res., 104, 26,525–26,545, 1999.
- Ruhnke, R., W. Kouker, T. Reddmann, H. Berg, G. Hochschild, G. Kopp, R. Krupa, and M. Kuntz, The vertical distribution of ClO at Ny-Alesund during March 1997, *Geophys. Res. Lett.*, 26, 839–842, 1999.
- Russell, J. M., L. L. Gordley, J. H. Park, S. R. Drayson, A. F. Tuck, J. E. Harries, R. J. Cicerone, P. J. Crutzen, and J. E. Frederick, The halogen occultation experiment, *J. Geophys. Res.*, 98, 10,777–10,797, 1993.
- Sander, S. P., et al., Chemical kinetics and photochemical data for use in stratospheric modeling, supplement to evaluation 12: Update of key reactions, JPL Publ., 00-3, 2000.
- Sasano, Y., M. Suzuki, T. Yokota, and H. Kanzawa, Improved Limb Atmospheric Spectrometer (ILAS) for stratospheric ozone layer measurements by solar occultation technique, *Geophys. Res. Lett.*, 26, 197–200, 1999.

- Schulz, A., et al., Match observations in the arctic winter 1996/97: High stratospheric ozone loss rates correlate with low temperatures deep inside the polar vortex, *Geophys. Res. Lett.*, 27, 205–208, 2000.
- Sugita, T., et al., Validation of ozone measurements from Improved Limb Atmospheric Spectrometer (ILAS), *J. Geophys. Res.*, 107, 10.1029/2001JD000602, in press, 2002.
- Swinbank, R., and A. O'Neill, A stratosphere-troposphere data assimilation system, *Mon. Weather Rev.*, 122, 686–702, 1994.
- Van den Broek, M. M. P., A. Bregman, and J. Lelieveld, Model study of stratospheric chlorine activation and ozone loss during the 1996/1997 winter, J. Geophys Res., 105, 28,961–28,977, 2000.
- Wamsley, P. R., et al., Distribution of halon-1211 in the upper troposphere and lower stratosphere and the 1994 total bromine budget, *J. Geophys. Res.*, 103, 1513–1526, 1998.
- G. Carver, Centre for Atmospheric Science, Department of Chemistry, Cambridge University, Cambridge CB2 1EW, England, UK. (glenn. carver@atm.ch.cam.ac.uk)
- J.-U. Grooß, G. Günther, P. Konopka, and R. Müller, Institute for Stratospheric Chemistry (ICG-1), Forschungszentrum Jülich, D-52425, Jülich, Germany. (j.-u.grooss@fz-juelich.de; g.guenther@fz-juelich.de; p.konopka@fz-juelich.de; danny@acd.ucar.edu; ro.mueller@fz-juelich.de) D. S. McKenna, Atmospheric Chemistry Division, NCAR, 1850 Table Mesa Drive, Boulder, CO 80307–3000, USA. (danny@ucar.edu)
- Y. Sasano, Global Environment Division, National Institute for Environmental Studies, Tsukuba, Ibaraki, 305-0053, Japan. (sasano@nics.go.jp)

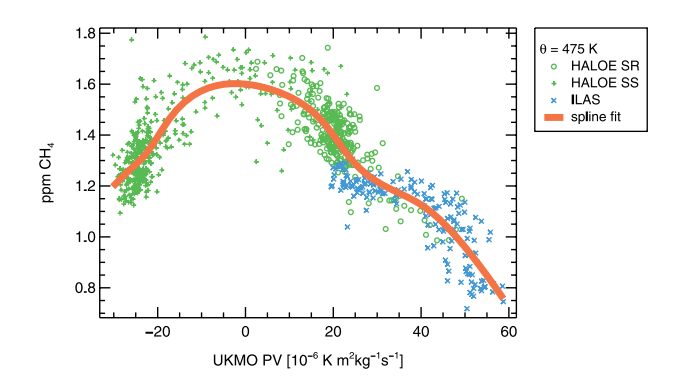


Figure 1. CH₄ initialization on 20 February 1997. Green symbols depict Halogen Occultation Experiment (HALOE) sunset data at $\theta = 475$ -K potential temperature level between 16 February and 17 March 1997 and sunrise data between 16 February and 9 March 1997. Blue symbols show CH₄ mixing ratios derived from Improved Limb Atmospheric Spectrometer (ILAS)N₂O data between 13 and 27 February and from the N₂O/CH₄ correlation in Table 4. Potential Vorticity (PV) of the individual data points is determined by trajectory simulations from the measurements location to 20 February 1997. Also shown is a spline fit to the data that are used for initialization.

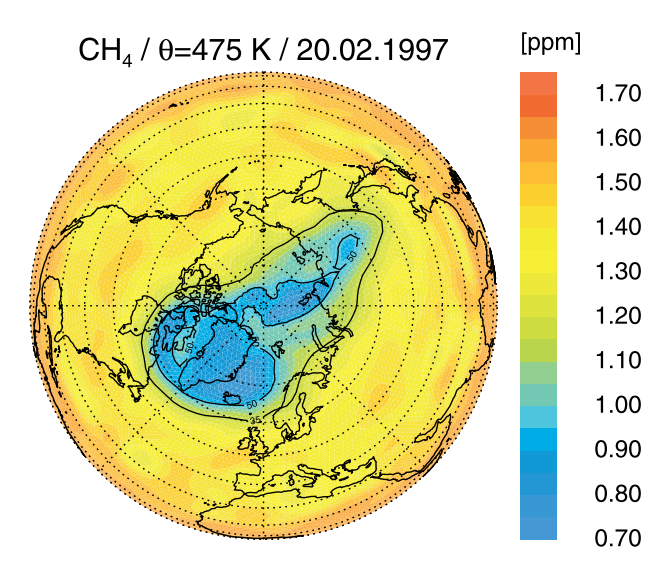


Figure 2. Initialization for CH₄ derived from spline fit correlation with PV on the 475-K potential temperature level mapped on an orthographic projection. Black lines mark the PV contour for 35 PV units (PVU) (vortex edge) and 50 PVU (vortex core region).

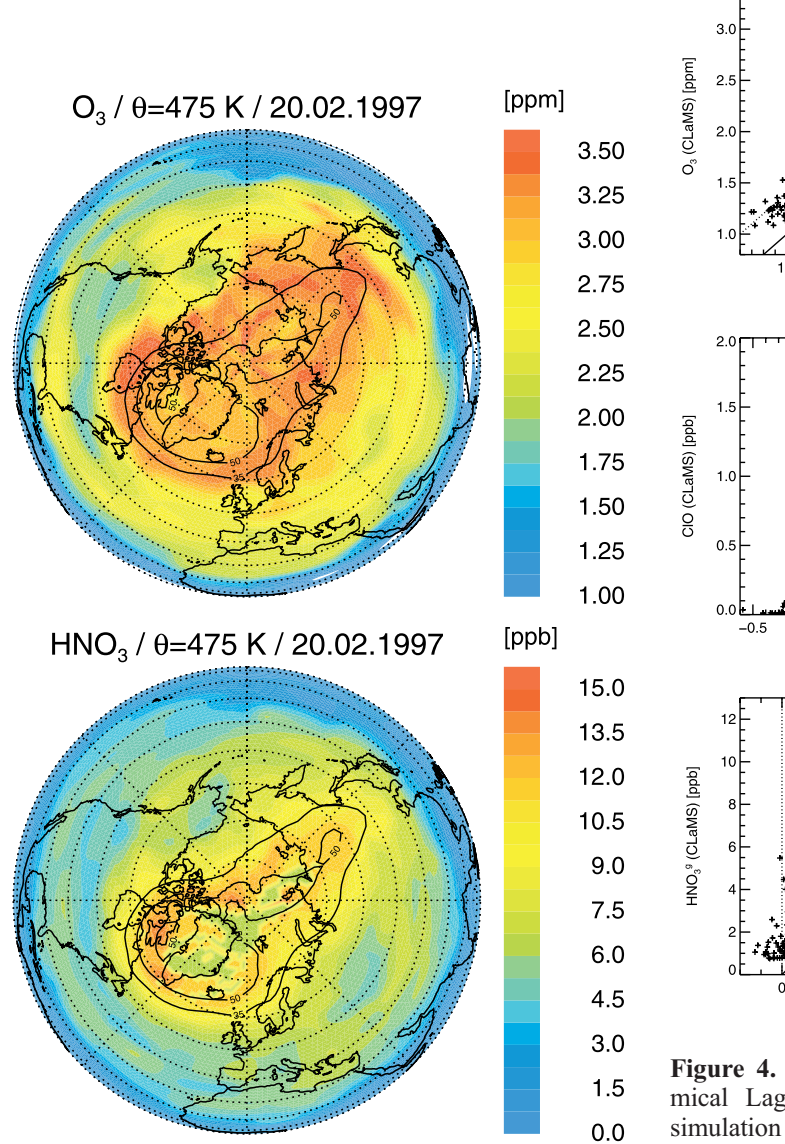


Figure 3. Initialization for (top) O₃ and (bottom) HNO₃ on the 475-K potential temperature level mapped on an orthographic projection. Ozone data are derived from HALOE, ILAS and Microwave Limb Sounder (MLS) data sets, whereas HNO₃ is derived exclusively from MLS. PV contour lines for 35 and 50 PVU are shown in black.

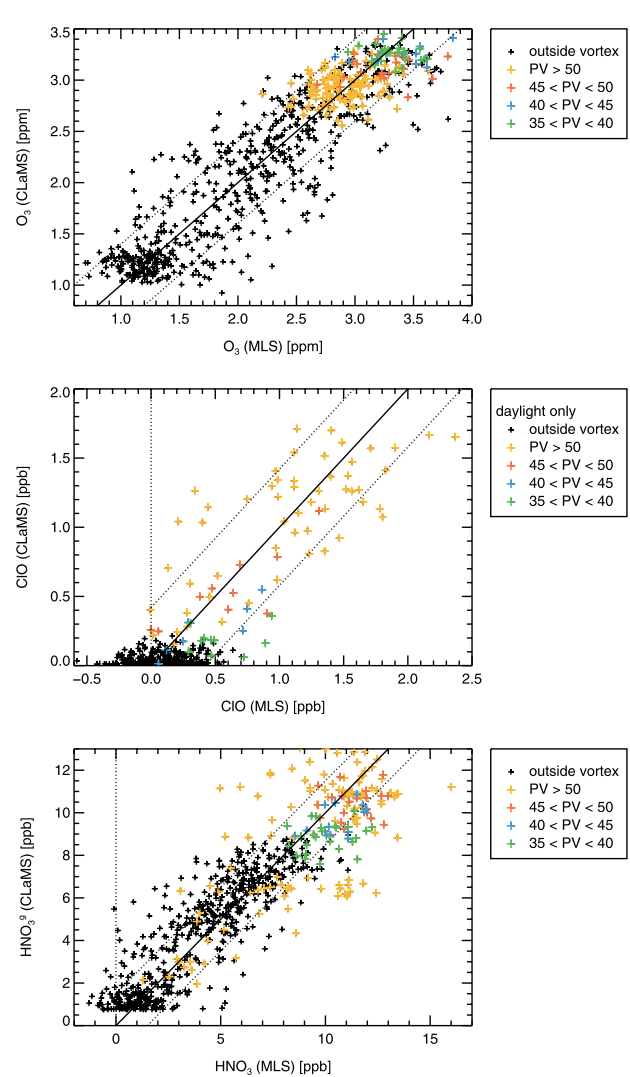


Figure 4. Comparison MLS observations with the Chemical Lagrangian Model of the Stratosphere (CLaMS) simulation for 26 February 1997 for (top) O₃, (middle) ClO, and (bottom) gas-phase HNO₃. MLS observations are plotted against CLaMS simulations for the location and time of the MLS observations. Vortex observations are shown in different colors for different PV. Outside vortex observations are plotted as black symbols. One-to-one line is plotted as a solid line, and the given MLS accuracy is indicated by the dotted lines.

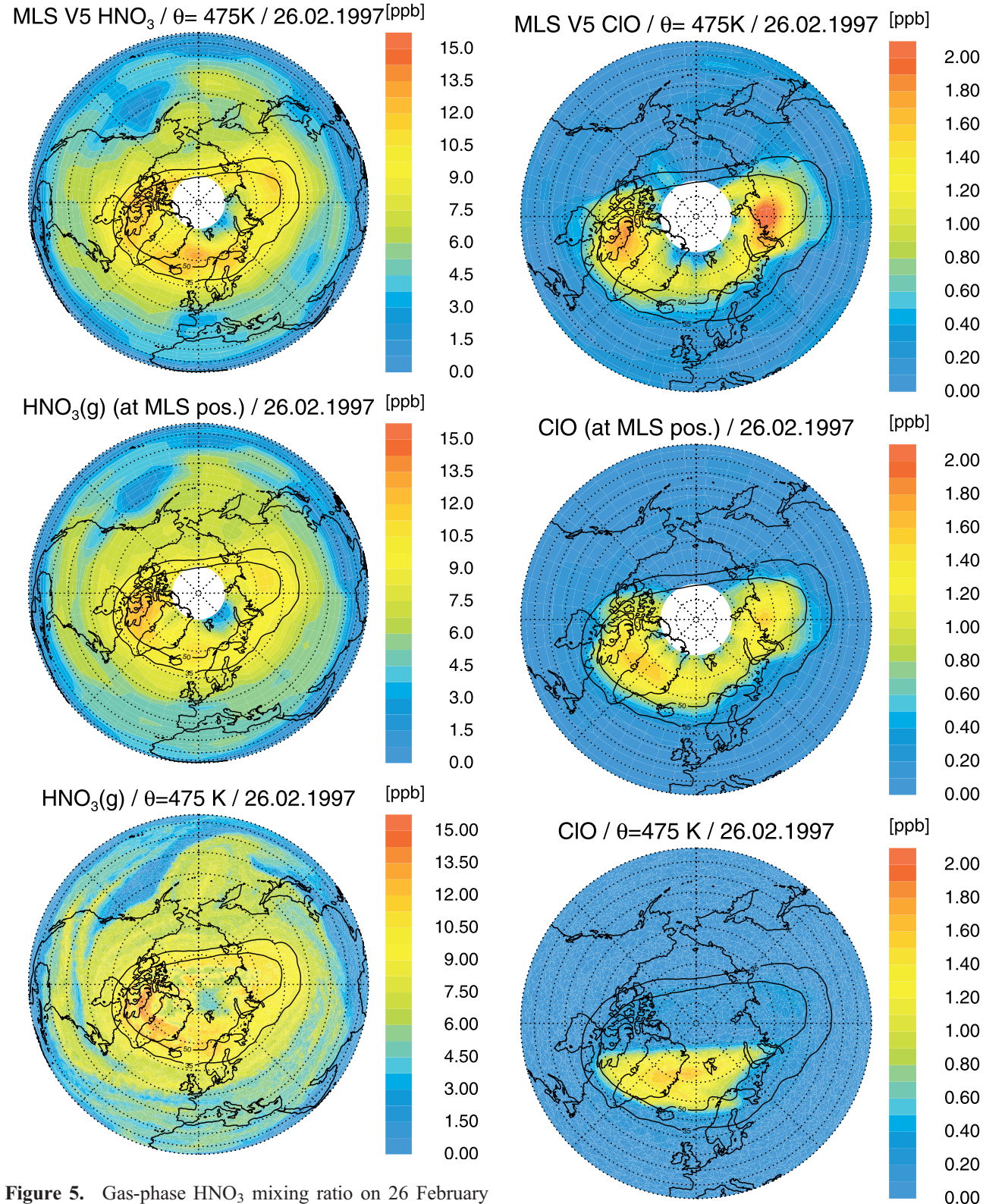


Figure 5. Gas-phase HNO₃ mixing ratio on 26 February 1997. (top) MLS measurements as typically plotted. (middle) Model results of the same locations in space and time as the MLS observations, plotted with the same gridding procedure as above. (bottom) Model results for full CLaMS resolution.

Figure 6. As in Figure 5, but for ClO mixing ratio. (top) Daytime MLS measurements (between 0800 and 1900 local solar time). (middle) Model results for the MLS positions. (bottom) Model results at 1200 UTC for full resolution.

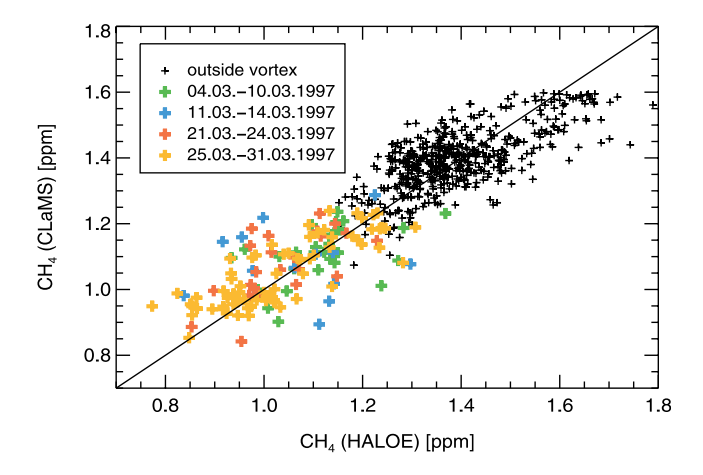


Figure 7. Comparison of CH₄ mixing ratios observed by HALOE with the CLaMS simulation for all HALOE data points within the simulation period. Vortex observations are shown in different colors indicating the time of the observation. Outside vortex observations are plotted as black symbols.

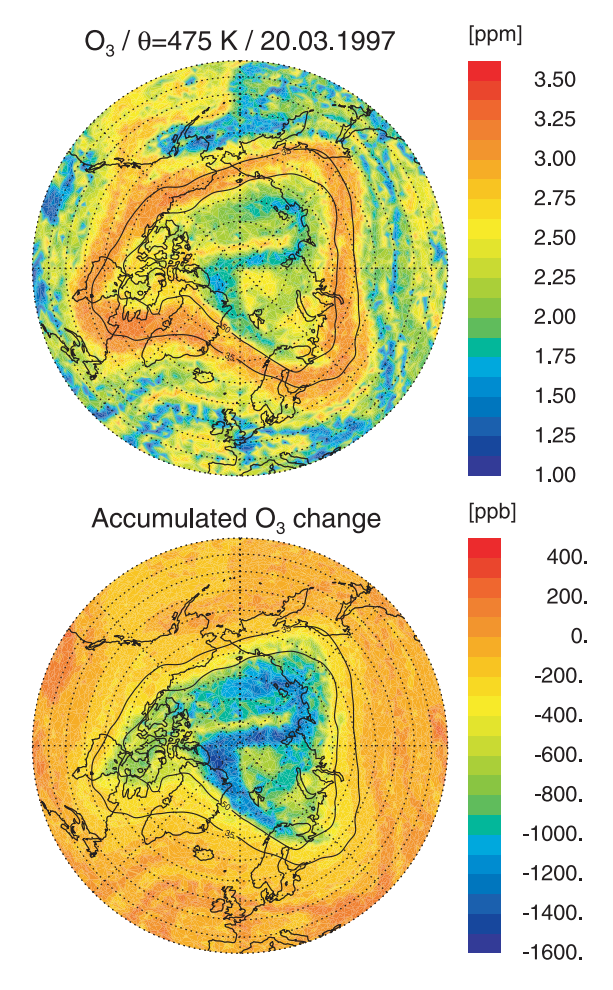


Figure 8. Results of the simulation for 20 March 1997 on the 475-K isentropic level. (top) Simulated ozone mixing ratio. (bottom) Accumulated chemical ozone change since 20 February 1997.

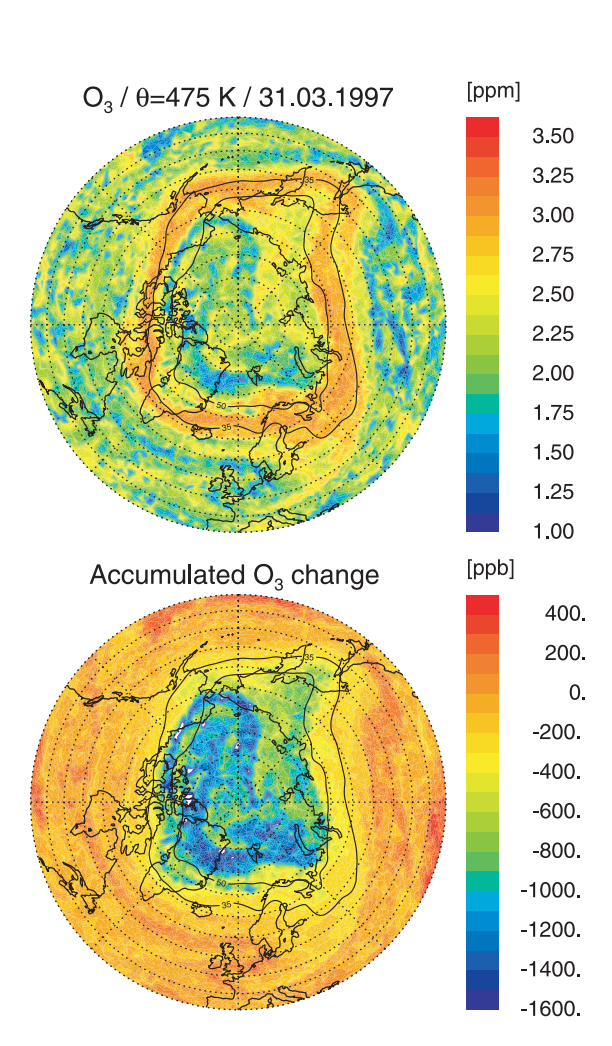


Figure 9. As in Figure 8, but for 31 March 1997.

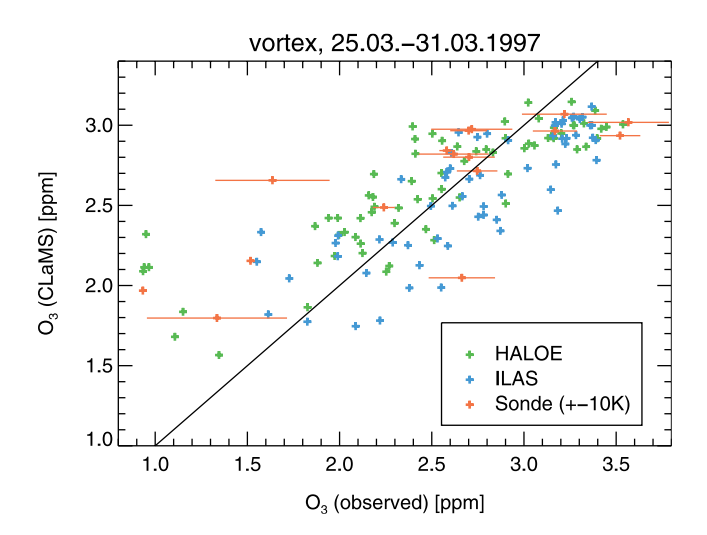


Figure 10. Comparison of O_3 mixing ratios observed by HALOE, ILAS, and ozone sondes within the last week of the CLaMS simulation (25–31 March 1997). For the ozone sondes (red symbols) the average standard deviation in the interval $\theta = 475 \pm 10$ K is depicted. One-to-one line is plotted as a solid line.

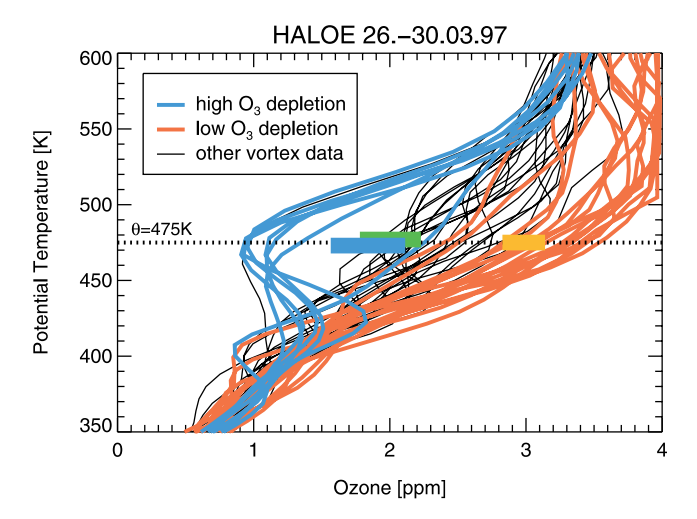


Figure 11. HALOE ozone profile measurements inside the vortex between 26 and 30 March 1997. Color indicates the simulated ozone depletion. Blue lines show HALOE data at locations of high ozone depletion, red lines show HALOE data at locations of low ozone depletion, and black lines show the remaining vortex data (see text for details). Colored bars show the range of the simulated ozone mixing ratios interpolated to the HALOE measurement locations. Blue bar corresponds to the blue HALOE profiles for the reference simulation with denitrification. Green bar corresponds to the same for the sensitivity calculation without denitrification. Orange bar corresponds to the red HALOE profiles (for simulations both with and without denitrification).